UNIVERSITY OF IOANNINA

MSc THESIS

Study of the acetylene photooxidation reaction in the 280-325 nm spectral range

---

Author:
Papigkiotis Iraklis Marios
Identification number: 784

Supervisor:
Sofikitis Dimitrios

A thesis submitted in fulfillment of the requirements
for the Master in Science"Postgraduate Studies in Physics"

of the

University of Ioannina
Physics Department

September 28, 2023

Acknowledgements

To begin with, i would like to express my sincere gratitude to my supervisor, Dimitrios Sofikitis, for his invaluable guidance and support throughout my master's program. Moreover, a worthy reference must also be made to the Professor Konstantinos Kosmidis for the advice and guidance he offered during the project helping me overpass difficulties regarding the experimental apparatus. I would also like to thank the members of the lab Alexis, Manos, Panos for the great teamwork and our involvement with various side projects such as the "A.R.B" project. I would like to thank my friends for their love and support during this process as well my girlfriend Katerina for her understanding and support during these years. Finally, the greatest gratitude I owe to my parents Vasiliki and Stephanos and to my siblings Gregory, Stavros, Maria-Louiza for their support and encouragement throughout all these years.

UNIVERSITY OF IOANNINA

Abstract

University of Ioannina
Physics Department

Master in Science

Study of the acetylene photooxidation reaction in the 280-325 nm spectral range

by Papigkiotis Iraklis Marios Identification number: 784

In this work, we studied the photooxidation of acetylene throught the glyoxal creation channel in the spectral region $280 - 325\ nm$. A ns multiphoton ionization study in this region revealed 2 major lines attributed to the partially dissociating (Herzberg type II pre-dissociation) Valence state $\tilde{C}'^1A_g$ with lifetime of around 1 ps. The impact of this state to the phootoxidation mechanism of acetylene is considered negligible compared to the impact of the pre-dissociative Rydberg states $\tilde{C}^1\Pi_u$ and $3p^1\Pi_g$ (with lifetime of around 50 fs) although absent in typical ionization studies. The photooxidation of acetylene is believed to occur in the early stages of the fragmentation process of the parent molecule after excitation to the aforesaid pre-dissociating Rydberg states. The creation of C_2H radicals seems to initiate the glyoxal production (the more the dissociating channel produces C_2H radicals, the more the reactivity gets maximized). The reaction is supposed to proceed via a four-membered ring re-arrangement of the C_2H radical with the molecular Oxygen (during the pre-dissociation process) in the molecular skeleton and with the addition of a free Hydrogen, glyoxal is created.

Contents

List of Figures

Chapter 1

Introduction

The acetylene molecule, the simplest unsaturated hydrocarbon, is an important starting material in the creation of various organic compounds such as plastics, pharmaceuticals, and chemicals [1]. In terms of spectroscopy, Acetylene gas is applied in analytical chemistry and as a fuel material and carbon source, due to the fact that acetylene is very flammable, in flame tests [2]. Is is also widely present in both the interstellar medium and planetary atmospheres [3]. Its abundant presence and distinctive spectral characteristics make observations of acetylene a significant tool for studying the atmospheric chemistry of planets and moons within our solar system [4], [5], [6], [7]. Additionally, acetylene, along with the ethynyl radical, plays a crucial role in hydrocarbon combustion and the formation of soot [8].

When acetylene undergoes oxidation, it produces a great variety of products, including carbon monoxide, carbon dioxide, formaldehyde, glyoxal, formic acid, hydrogen, and water [9]. Among these products, glyoxal stands out due to its status as a Volatile Organic Compound (VOC), which can be detected both easily and remotely. Due to its relatively short lifetime in the atmosphere, glyoxal serves as a valuable indicator of local photochemical activity [10], [11]. Notably, nearly 20% of atmospheric glyoxal originates from the oxidation of acetylene [12] while the rest is still unknown. Recent investigations highlight the uncertainty surrounding the source of elevated glyoxal concentrations over equatorial oceans [10].

The focus of this research lies in examining the rate at which glyoxal forms through the photooxidation of acetylene [4]. This investigation is conducted using acetylene/oxygen mixtures at room temperature and employing tunable laser UV radiation. Previous studies using thermal UV sources [13] or non-tunable excimer laser radiation [14], [15] did not provide insights into how discrete excited states impact the photooxidation process. In this study, two photooxidation pathways are identified, corresponding to the excitation of either the excited Rydberg state $\tilde{C}^1\Pi_u$ or the $3p^1\Pi_g$ Rydberg state [16]. Both states, with an excitation energy falling within the VUV (Vacuum Ultraviolet) region, are accessed through a two-photon absorption process. Due to its rapid predissociation, these states cannot be detected in ns multiphoton ionization experiments. This research underscores the significance of highly-excited Rydberg states, which, although not readily observable in typical photoionization experiments, play a vital role in acetylene's photochemistry.

Ultimately, the involvement of excited states in various photo-induced reactions has the potential to impact the behavior of reactions. This insight could aid in understanding observed VOC planetary budgets and astrochemical phenomena.

The purpose of this work is to study the role of predissociation and non-dissociating states in the laser induced photooxidation of acetylene by using tunable radiation in the range of $280 - 325\ nm$. An outlook of the thesis is the following:

- Chapter 2 explains some molecular physics elements that are needed throughout the study.
- Chapter 3 describes the experimental apparatus of our experiments.
- Chapter 4 contains the results and the discussion that leads to the description of the photooxidation mechanism.
- Chapter 5 pinpoints the conclusions of our study and some interesting proposals for further study.

Chapter 2

Elements of molecular physics

2.1 Molecular Valence - Rydberg states

Molecular valence states are electronic configurations involving the outermost electrons. In terms of chemical bonding, these electrons play a crucial role in determining the chemical and reactivity properties of the molecules. In a molecule, one or more valence electrons can be promoted into higher electronic states (in terms of energy). The excited states can be divided into 2 main groups: excited Valence states, excited Rydberg states. As far as atomic physics is concerned, Rydberg states are characterized by the large principal number n (50-100) and the atom's behaviour (after excitation to such state) approaches assymptotically the behaviour of the corresponding cation [17], while its energetics can be approximated using the Rydberg formula:

$$\frac{1}{\lambda_e} = R_H\left(\frac{1}{n_1^2} - \frac{1}{n_2^2}\right) \tag{2.1}$$

with n_1, n_2 being the principal quantum number of the electronic states that participate in the transition, R_H the Rydberg constant and λ_e the wavelength of the emitted radiation. In contrast, molecular Rydberg states are states with much lower principal number n where, due to the extra degrees of freedom (including vibrations and rotations), a mixing of the excited electronic-rovibronic states approaches some kind of continuum of states similar to the atomic case. The molecular Rydberg states are severely more complicated than atoms due to the presence of more than one nuclei [18]. Therefore, a theory is required to handle the presence of bound and slowly fragmenting states in a compact way.

For Rydberg alkali atoms the energy can be given by the approximated formula:

$$E_{nl} = I - \frac{R_y}{(n-\mu_l)^2} \tag{2.2}$$

where E_{nl} being the energy of the Rydberg state, I the ionization potential of the atom, R_y the Rydberg energy constant, n the principal quantum number and μ_l the quantum defect. On the other hand, the corresponding energy for the molecular Rydberg states can be expressed in a first approximation with the following formula

[18] (for a simple diatomic molecule) :

$$V_{nl\lambda} = V^{+}(R) - \frac{R_y}{(n-\mu_l)^2} \tag{2.3}$$

where $V_{nl\lambda}$ being the ab initio potential function for principal quantum numbers and $V^{+}(R)$ being the potential energy as a function of the inter-nuclear distance of the positive ion [19]. Such formulae [19] can predict with high-precision low-lying potential energies for small molecules, including Rydberg states up to $n = 4$. However, the extension to higher members of the series is prohibitive due to the very diffuse outer parts of the orbitals which cannot be approximated correctly with Gaussian functions. In contrast, Molecular Quantum Defect Theory (MQDT) techniques which use exact Coulomb wave functions in the asymptotic region, take into account the necessary interactions with the nuclei can extract quantum defect functions from the molecular analogue of Eq. 2.2 and predict the energy levels in states with n>4.

2.2 Selection rules

After a brief description of the Valence and Rydberg states, it is time to mention the selection rules which determine whether an optical transition is permitted or not. Before we begin, we explain the terminology of gerade and ungerade which refer to the symmetry of the wavefunction [20].

Gerade and ungerade states, respectively, are some of the terms commonly used in molecular spectroscopy in order to describe the symmetry properties of molecular electronic states under the action of certain symmetry operators regarding molecules which possess a center of inversion.

As gerade, we symbolize the electronic states that exhibit symmetry with respect to the inversion around the molecule's center of symmetry. In simple words, if the molecule is inverted through its center then the wavefunction describing the electronic state stays intact or is symmetric. On the other hand, ungerade states are electronic states that do not exhibit symmetry with respect to the inversion around the molecules' center. In such states, the inversion through the center of symmetry of the molecule gives rise to a sign change in the wavefunction, the so-called antisymmetric wavefunction. Therefore, we can infer if an electronic state is either gerade or ungerade by inverting the molecule around a plain perpendicular to the molecular axis and checking if the wavefunction maintains its sign as shown on Figure 2.1 regarding linear molecules.

The study of both gerade and ungerade states play a significant role in the understanding of the electronic and vibrational properties of molecules. The symmetry properties of these states influence their behavior upon excitation by giving rise to certain selection rules, which lead to characteristic patterns in molecular spectra.

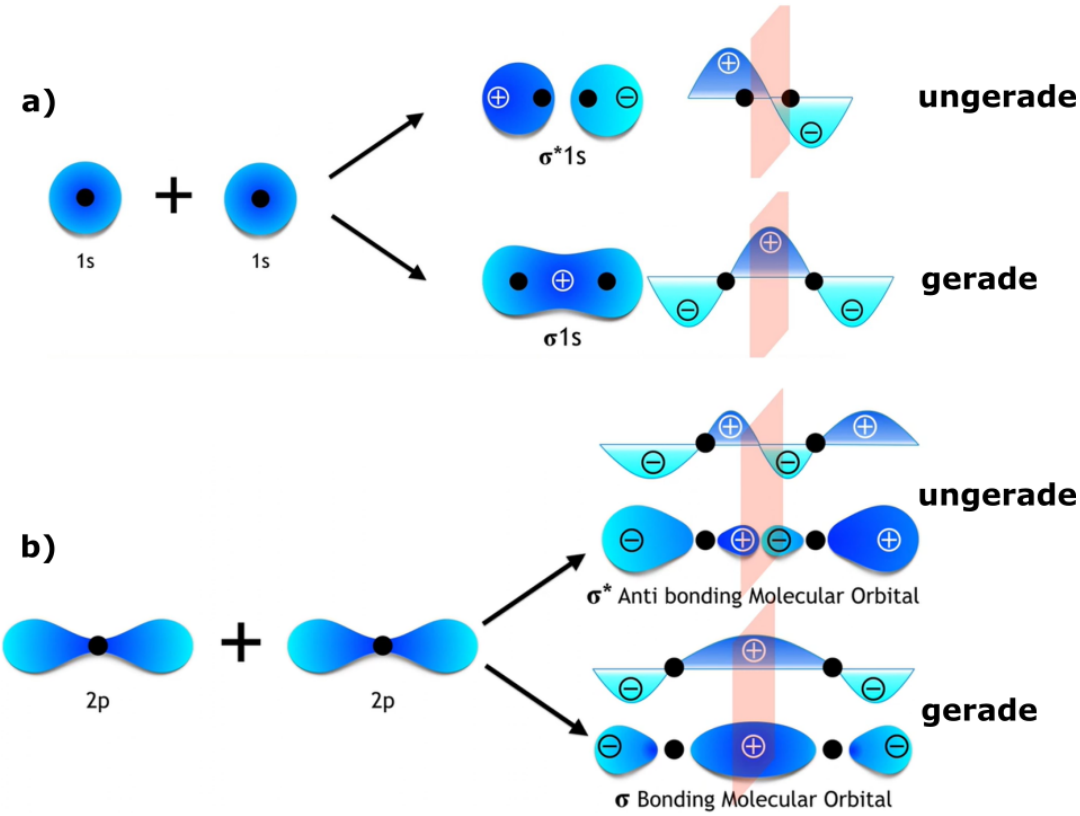

FIGURE 2.1: Qualitative representation of gerade and ungerade states in the mixing of a) $1s$ orbitals and b) $2p_x$ orbitals in a homonuclear diatomic molecule.

In order to study the structure of molecules via electronic spectroscopy, one has to understand the conditions under which the transition from the initial to the final state is attainable. We assume a molecule in the framework of the Born-Oppenheimer approximation [21] where the nuclei are assumed to be fixed due to the fact that nuclei are much heavier compared to the electrons and therefore the wavefunction of the electrons can be treated separately. The total wavefunction can be expressed as a product of an electronic Ψ_{el} and a vibrational Ψ_{vib} part as follows:

$$\Psi_{tot} = \psi_{el}(r)\psi_{vib}(R) \tag{2.4}$$

where r shows the distance of the electron from the molecules' center of mass and R being the distance between the atoms that participate in the vibration. In order to calculate the transition rates, we introduce the electric dipole operator as follows:

$$\hat{\mu} = \sum_i q_i \hat{r}_i \tag{2.5}$$

with q_i being the charge of each individual electron and $\hat{r}_i$ the distance from the center of mass. The transition dipole moment is equal to:

$$R_{21} = \int \psi_2^* \hat{\mu} \psi_1 d\tau = \langle \psi_2 | \hat{\mu} | \psi_1 \rangle \tag{2.6}$$

with $d\tau$ being the volume element. By combining Eq. 2.4 and 2.6, the transition dipole operator R_{21} becomes

$$R_{21} = -e \int \psi'^{*}_{el}(r) r \psi''_{el}(r) dr \int \psi'^{*}_{vib}(R) r \psi''_{vib}(R) dR \tag{2.7}$$

where the notations ψ', ψ'' corresponds to ψ_2, ψ_1 respectively. The first integral of Eq. 2.7 refers to the electronic transition moment, while the second integral is the vibrational overlap of the participating vibrational states. The transition probability is proportional to the quantity

$$R_{21}^2 \propto \left(\int \psi'^{*}_{el}(r) r \psi''_{el}(r) dr \right)^2 \left(\psi'^{*}_{vib}(R) r \psi''_{vib}(R) dR \right)^2 \tag{2.8}$$

where the second factor is the Frank-Condon factor expressing the square of the vibrational overlap integral. The first factor gives rise to the selection rules regarding the electronic transitions as:

$$\begin{gathered} \Delta\Lambda = 0, \pm 1 \\ \Delta S = 0 \; and \; \Delta\Sigma = 0 \\ g \leftrightarrow u \; (where \; g, \; u \; exist) \\ + \leftrightarrow +; \; - \leftrightarrow - \; (for \; \Sigma - \Sigma \; transitions) \end{gathered} \tag{2.9}$$

where $\Lambda = \sum_i \lambda_i$ is the overall angular momentum on the intenuclear axis and Σ is the projection of S on the internuclear axis (see Figure 2.2).

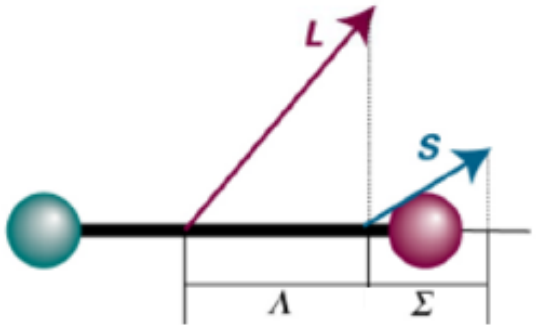

FIGURE 2.2: Qualitative representation of L and S projected on the internuclear axis giving rise to Λ and Σ respectively.

For centrosymmetric molecules, the two-photon selection rules can be expressed as:

$$g \leftrightarrow g \; and \; u \leftrightarrow u. \tag{2.10}$$

Although the selection rules come from the transition between the electronic states, the Frank-Condon factor determines the strength of the transition [20]. For

simplicity reasons, we refer to diatomic molecules. As mentioned before, the Frank-Condon factor strongly depends on the overlap of the vibrational part of the wave-functions of the initial and final state which introduces a further dependency on the geometry of the participating states.

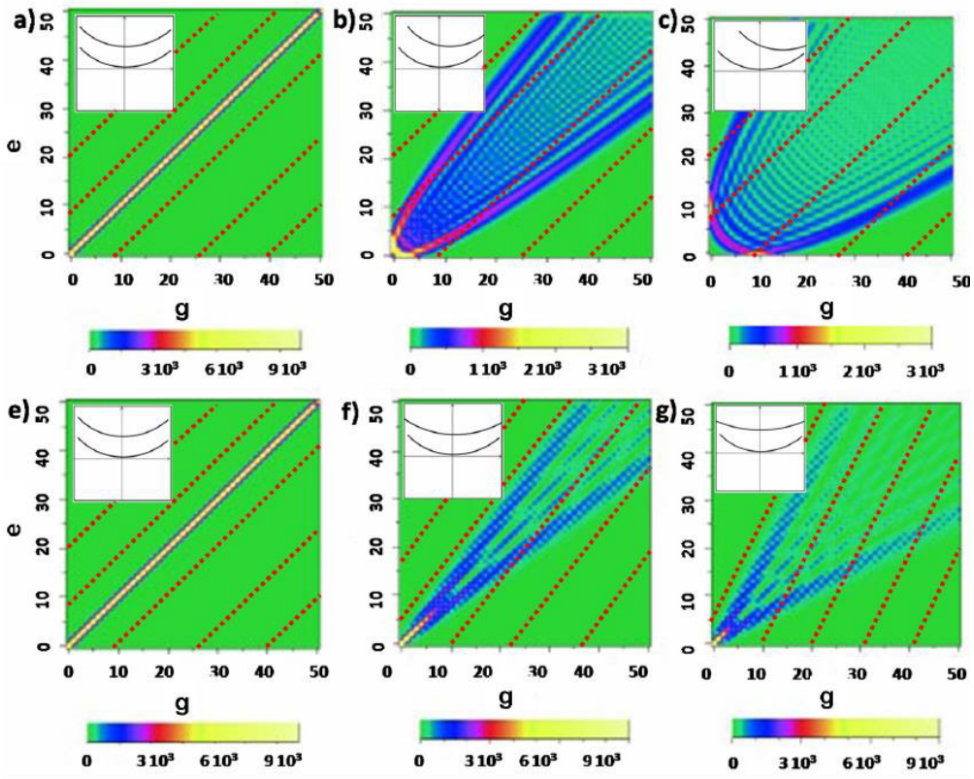

FIGURE 2.3: Plots of Frank-Condon values for different shapes and equilibrium geometries between the states participating in the transition. The transition probability is expressed as a coloured map while the vertical axis refer to the vibrational levels of upper and lower states [22], [23].

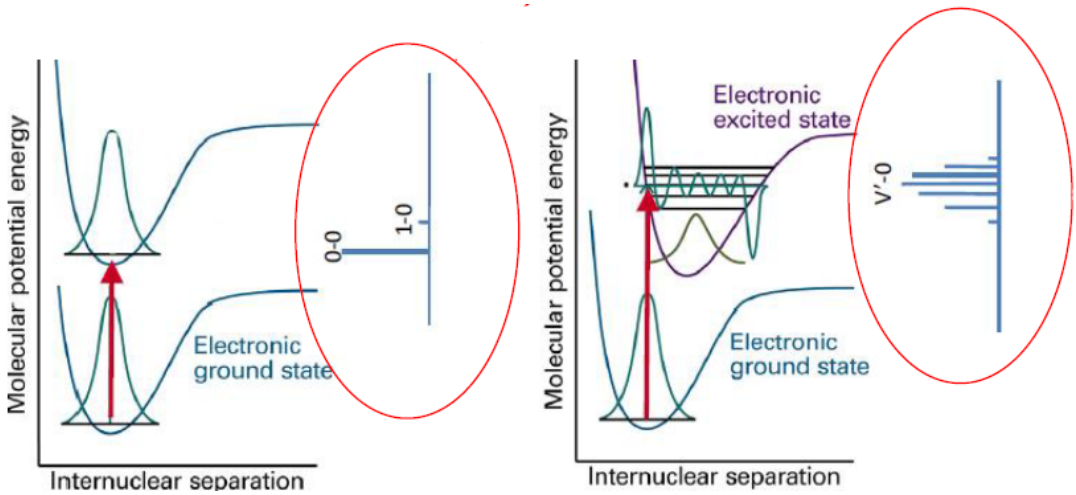

FIGURE 2.4: Qualitative representation of short (long) progression that gives gives rise to poor (rich) spectra [24].

Supposing that the upper and lower potential wells are similar (similar equilibrium geometry and depth), the vibrational wavefunctions are almost the same which means that transitions occur between states of the same ν giving rise transitions with $\Delta\nu = 0$ being the strongest transitions and the mapping of the Franck-Condon values (see Figure 2.3) gives rise to the shape of a line with a 45° slope. Now, imagine that the upper state has a similar potential well but centered at a bigger equilibrium geometry ($R_{upper} > R_{lower}$). The $\nu = 1$ upper vibrational level has a better overlap with the $\nu = 0$ lower vibrational level as the vibrational part of the wavefunction is the same but shifted towards the right. In this case, the mapping of the Frank-Condon values has the shape of a parabola. For different equilibrium geometries between the states and different shapes of the potential well, this parabola changes shapes giving rise to the so-called Frank-Condon parabola. Examples of the various Frank-Condon parabola are shown on Figure 2.3.

The study of the absorption spectra of such transitions can help us explain the structure of the excited states. Figure 2.3a represents 2 states with similar quantum wells. In this cases, the spectrum contains very few, lines, due to the very small overlap between vibrational wavefunctions of different ν vibrational levels [22]. On the other hand, the difference on the geometry of the 2 states, gives rise to non-zero transition probabilities of multiple vibrational levels leading to a rich spectra. These two categories of spectra are called short and long progression spectra and are useful indicators of the geometry changes during an electronic transition (see Figure 2.4). M. Takahashi [25], using a 2 color double resonance spectroscopy, studied the geometry of the $\tilde{A}^1A_u$ excited valence state of acetylene from the long progression that appeared in the spectra.

Now, for a purely vibrational transition occurring in the same electronic state, the description is simplified [22]. The selection rule in this case applies as $\Delta\nu = \pm 1$. For example, if a $\nu = 5$ vibrational level is occupied then, a step by step de-excitation will take place by the following vibrational transition: $\nu = 5 \rightarrow \nu = 4 \rightarrow \nu = 3 \rightarrow \nu = 2 \rightarrow \nu = 1 \rightarrow \nu = 0$. Though, in reality the $\Delta\nu = \pm 1$ selection rule is not that strong which gives rise to the so-called overtones $\Delta\nu = \pm 1, \pm 2, \pm 3$.... Every overtone appearing is weaker than the previous by approximately an order of magnitude.

This sub-section will close by mentioning as well the selection rules regarding the rotational degrees of freedom [22]. In order for a purely rotational spectra to exist, the molecule must have a permanent dipole moment. Going back again to the Fermi's Golden rule, the selection rules regarding the quantum numbers of the angular momentum due to rotation comes out as:

$$\Delta J = \pm 1. \tag{2.11}$$

2.3 Dissociative states

In order to define the term "pre-dissociation" we must first refer to the potential energy surfaces of the excited states. Figure 2.5 illustrates qualitatively a slice of the potential energy surfaces of the ground state, an excited bound state and a dissociative state. These potential energy 'curves' describe the motion of only one atom in the polyatomic molecule and result from slices of the potential energy surfaces. The first 2 potential energy curves have a local minima which makes these 2 states "stable" while the latter does not possess such a minimum, which makes the state dissociative. Now, imagine an electronic transition from the ground state to the dissociative excited state. After such an excitation, the molecule will eventually be led to fragmentation. Not all dissociative states end up to the same fragments. In general, the dissociation channels may vary depending on the dissociative state. For the acetylene molecule, the dissociation channels are shown on Section 2.4. Regarding pre-dissociation, there is a chance that the potential curves cross at some point which is the case presented on Figure 2.5. A cross between an excited bound state and a dissociative state via conical intersection processes is capable of leading the molecule to dissociation. From now on, we will refer to this type of fragmentation as pre-dissociation.

Concerning the electronic, vibrational and rotational degrees of freedom of a molecule, one may distinguish 3 main cases of pre-dissociation according to Herzberg [26] namely:

- Case I: Pre-dissociation by electronic transition
- Case II: Pre-dissociation by vibration
- Case III: Pre-dissociation by rotation

The first case refers to the pre-dissociation by radiationless transition between the electronic state of one state with the continuum of another, while for the rest cases there is no change in the electronic state. Case II refers to the transition from a vibration to the continuum (see Figure 2.5), while case III pre-dissociation can occur in the transition from high rotational levels of a vibration to the continuum of the same vibration [26]. Case II cannot be met in diatomic molecules while case III has only been observed in diatomic molecules and it is unimportant for polyatomic molecules.

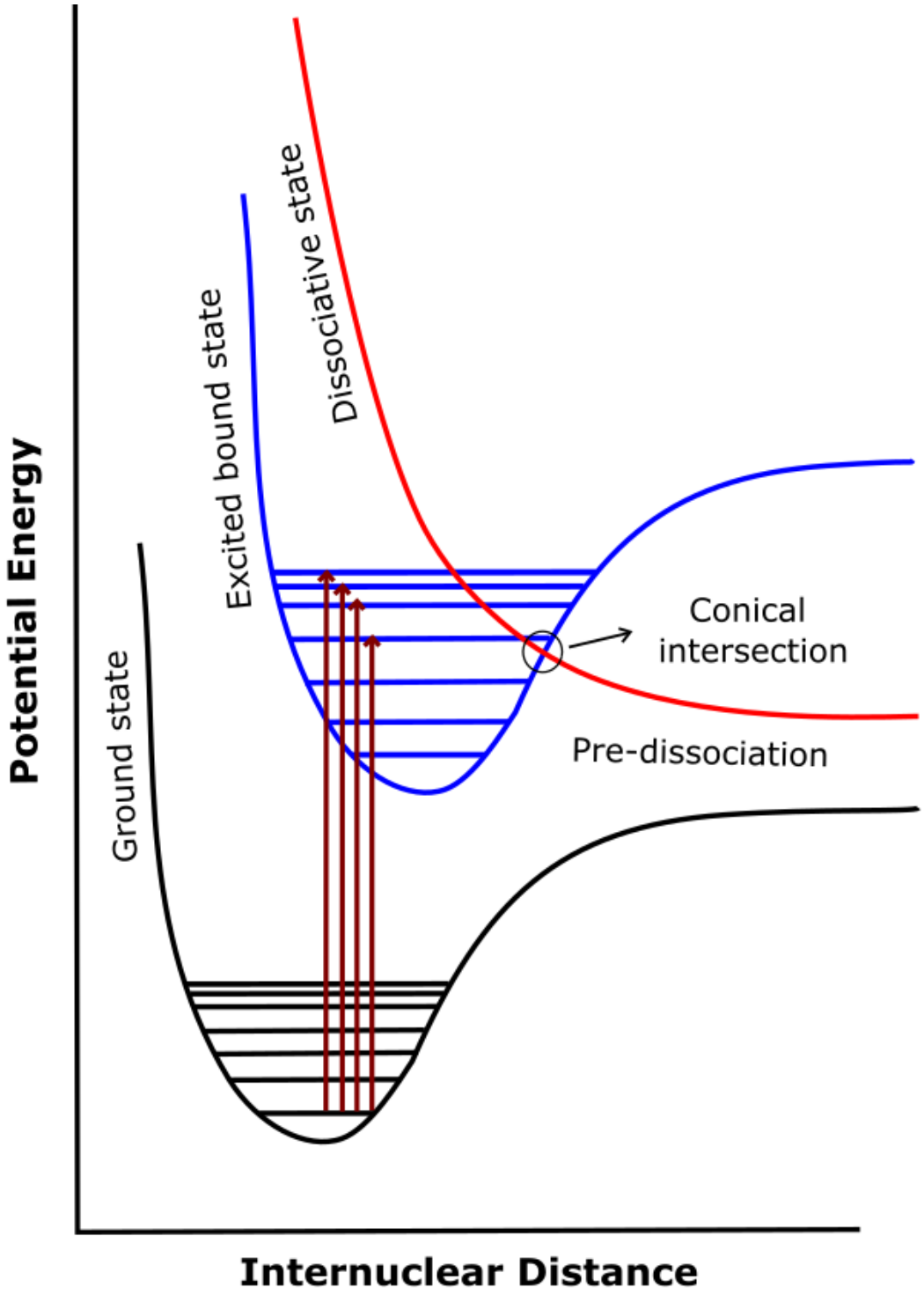

FIGURE 2.5: Qualitative representation of the pre-dissociation after conical intersection crossings of the excited bound state and the dissociative state.

2.4 Acetylene molecule

Acetylene is a highly reactive molecule with a chemical formula C_2H_2 and exhibits both Rydberg and valence molecular states, which play a crucial role in the understanding of both its chemical and spectroscopic behavior. Our study deals with the laser induced oxidation of acetylene (photooxidation). In order to explain the photooxidation mechanism, we have to describe the electronic states (Rydberg and Valence) accessed by our experiment which is also the content of this section. In particular, this section will be divided into 3 parts, each referring to different states according to this outline:

- Sub-section 2.4.1 will refer to the ground state of Acetylene and molecular Oxygen.
- Sub-section 2.4.2 will refer to the Rydberg states $\tilde{C}^1\Pi_u$ and $3p^1\Pi_g$ of Acetylene.
- Sub-section 2.4.3 will refer to the Valence states $\tilde{C'}^1A_g$ and $\tilde{A}^1A_u$ of Acetylene.

2.4.1 Ground state of Acetylene and Molecular Oxygen

According to [16], the ground state of Acetylene is the gerade singlet state $\tilde{X}^1\Sigma_g^+$ while the corresponding ground state of O_2 is the ungerade triplet state $X^3\Sigma_u^-$ [27]. Figure 2.6 shows not only the geometry of the ground state of both Acetylene and molecular Oxygen but also the distances between the atoms calculated by a simple geometry optimization in Avogadro [28]. Since these molecules are linear, they belong to the $D_{\infty h}$ point group [29] with ionization potential of 10.40 eV for Acetylene [16] and 12.06 eV for O_2[27]. Figures 2.7c, d show the HOMO orbital of the 2 molecules visualized with the help of Multiwfn [30], where the wavefunctions were built within GAMESS US[1] [32].

[1]Setting up and using these programs for the simpler case of atoms was the subject of my graduation thesis [31], and during my masters i developed further use of these programs to generate results for ground state molecules

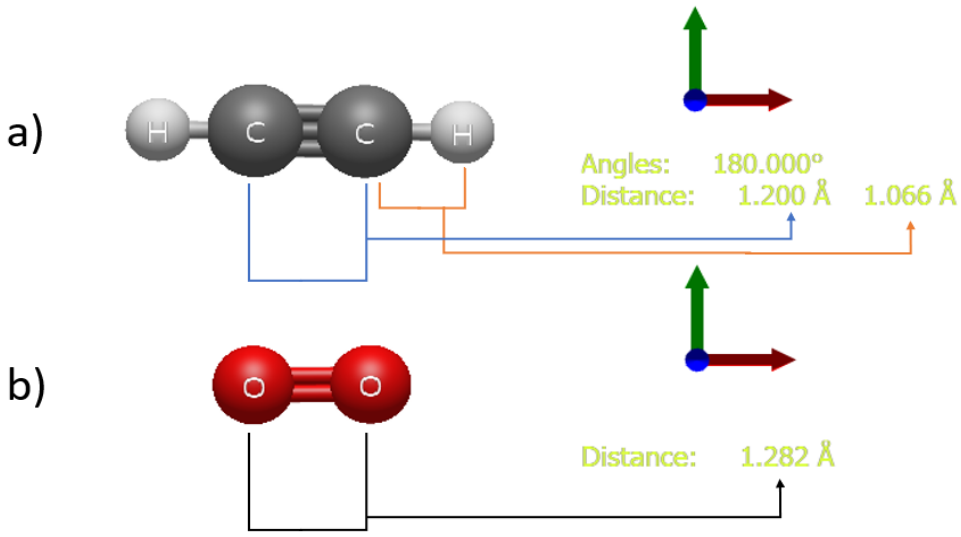

FIGURE 2.6: Schematic representation of the geometry of the ground state of a) Acetylene and b) molecular Oxygen including the distances of the atoms in the molecular skeleton calculated by a geometry optimization in Avogadro [28].

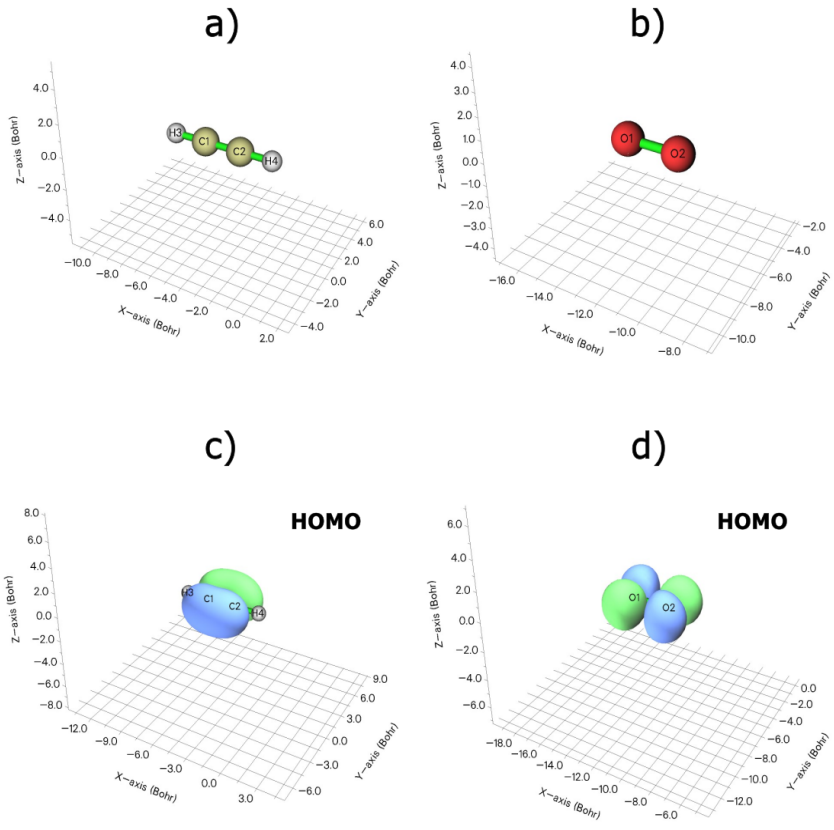

FIGURE 2.7: Schematic representation of the molecular skeleton of a) Acetylene, b) O_2 combined with their HOMO orbital on c), d) respectively.

2.4.2 Rydberg states $\tilde{C}^1\Pi_u$ and $3p^1\Pi_g$

After discussing first the ground state of Acetylene, we move on to the characterization of the excited (Rydberg) electronic states that appear to have impact on the photooxidation process and which are within reach with the dye lasers we are using.

One of the Rydberg states that appear to impact the photooxidation of acetylene is the electronic state $\tilde{C}^1\Pi_u$. According to the two-photon selection rules excitation from the (gerade) ground state should not be possible. However, there exist several low lying ungerade vibrations in the ground state [33] which can be populated in the conditions of our experiment, and which can be excited to the $\tilde{C}^1\Pi_u$ with two photon absorption.

The excitation to such a state does not change the geometry of the molecule, but the distances between the atoms in the molecular skeleton slightly changes. According to theoretical calculations presented in [16] for the Rydberg state $\tilde{C}^1\Pi_u$, the distances change to: $R_{CC} = 1.254$ Å and $R_{CH} = 1.073$ Å. Fabrice Laurelle and co-workers [16] mention the pre-dissosiating character of the $\tilde{C}^1\Pi_u$ Rydberg state which is confirmed in an extensive study made by Y. Zhang and co-workers [34] using the H-atom Rydberg tagging time-of-flight (HRTOF) technique at two excitation wavelengths in the VUV region.

In their work, below the first ionization limit they mention the 3 mainly dissociating channels where the C_2H_2 breaks down in the following fragments: C_2H, C_2, CH, H_2, H. The dissociating channels are shown below:

$$C_2H_2 \rightarrow C_2H + H,\ D_0 = 46074\ cm^{-1}, \tag{2.12}$$

$$C_2H_2 \rightarrow C_2 + H_2,\ D_0 = 50000\ cm^{-1}, \tag{2.13}$$

$$C_2H_2 \rightarrow CH + CH,\ D_0 = 79800\ cm^{-1}, \tag{2.14}$$

with the first channel being the dominating one according to [35].

In his work, Y. Zhang [34], found the lifetime of the $\tilde{C}^1\Pi_u$ excited state to be around 47 fs while the trans-bend vibration and rotation excitation of this state further reduces the lifetime ($22 - 39\ fs$) of the aforesaid electronic state leading to a faster dissociation process. The equilibrium geometry of the $\tilde{C}^1\Pi_u$ state of acetylene is linear which is also the case for the product $C_2H(\tilde{A}^2\Pi)$. From a dynamical point of view [34], a trans-bending vibrational excitation will make the Hydrogen atom leave the molecular skeleton in a non-linear way as shown on Figure 2.8 and the movemennt of the partner carbon in an opposite direction will enhance a bending excitation on the product $C_2H(\tilde{A}^2\Pi)$ which can be observed in Zhang's HRTOF experiment [34].

As far as this dissociation route is concerned, although there are some works proposing the exact path of the dissociation ([16], [34], [36],), the detailed energy surface crossing that effect the pre-dissociation of the $\tilde{C}^1\Pi_u$ state is still unknown.

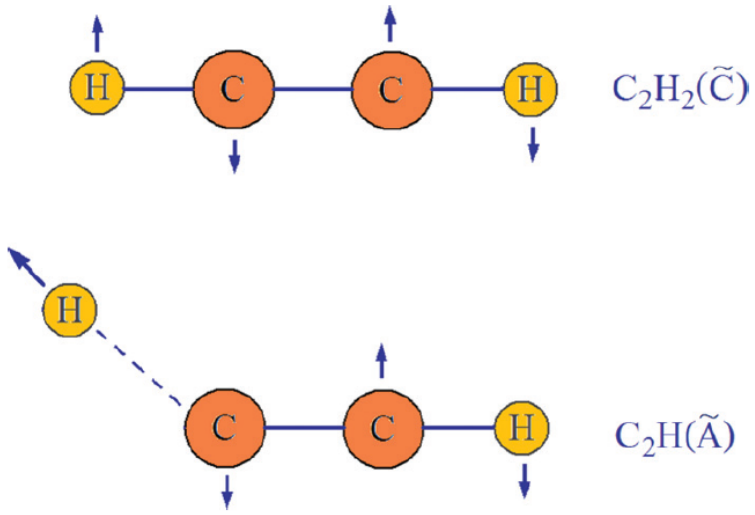

FIGURE 2.8: Schematic representation of the trans-bending of the C_2H_2 molecule during pre-dissociation resulting in the vibrationally excited product $C_2H(\tilde{A}^2\Pi)$.

On the other hand, the second Rydberg state within reach in our experiment is the $3p^1\Pi_g$ which, to the best of our knowledge, has yet to be observed experimentally. According to theoretical calculations ([16], [37]), the vertical energy of this state is around 8.4 eV and the molecule adopts a linear geometry with intemolecular distances between the atoms not so different compared to the $\tilde{C}^1\Pi_u$. The corresponding distances of the $3p^1\Pi_g$ state calculated in [16] are: $R_{CC} = 1.266$Å and $R_{CH} = 1.112$Å. Figure 2.9 shows a quantitative representation of the Rydberg molecular orbitals calculated by F. Laurelle and co-workers [16] where the blue (red) lines correspond to the negative (positive) values of the wavefunction in the isocontour map of step value 0.002.

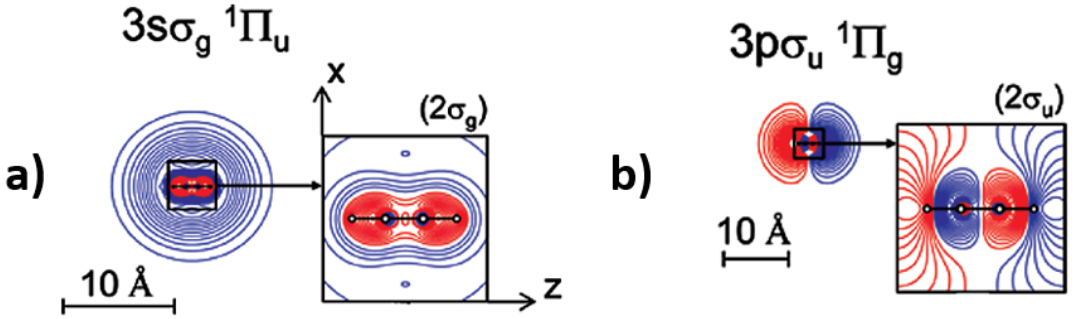

FIGURE 2.9: Quantitative representation of the Rydberg molecular orbitals of the a) $\tilde{C}^1\Pi_u$ and b) $3p^1\Pi_g$ Rydberg states. The blue (red) lines correspond to negative (positive) values of the wavefunction. The isocontour map was calculated by F. Laurelle's work [16] with an isovalue of 0.002.

2.4.3 Valence states $\tilde{C'}^1A_g$ and $\tilde{A}^1A_u$

The $\tilde{C'}^1A_g$ Valence state is within reach via a multiphoton absorption process (2+1 to ionization) in our experimental setup, so the theoretical and experimental background of such a state is important. Lundberg and co-workers [38] studied the

geometry of the $\tilde{C}'^1A_g$ excited state through Ultraviolet-Optical Double-Resonance spectroscopy (UVODR) by recording fluorescent spectra of the intermediate $\tilde{A}^1A_u$ state with a vertical energy of 5.23 eV calculated experimentally. At the same year, J. Lievin [39] using ab initio calculation, characterized theoretically the aforesaid Valence state, while more recent studies managed to characterize all the excited states [16]. The vertical energy of the excited state $\tilde{C}'^1A_g$ was found experimentally at 7.72 eV by Lundberg [38] while Laurelle [16] calculated the same state lying at 7.52 eV similar to the work done by Lievin [39]. M. Fujii and co-workers [40] using 3 different techniques (fluorescence excitation spectrum, MPI spectrum and absorption spectrum of the electronic transition $\tilde{A}^1A_u \leftarrow \tilde{X}^1\Sigma_g^+$) studied the $\tilde{A}^1A_u$ excited valence state which was found to be pre-dissociating.

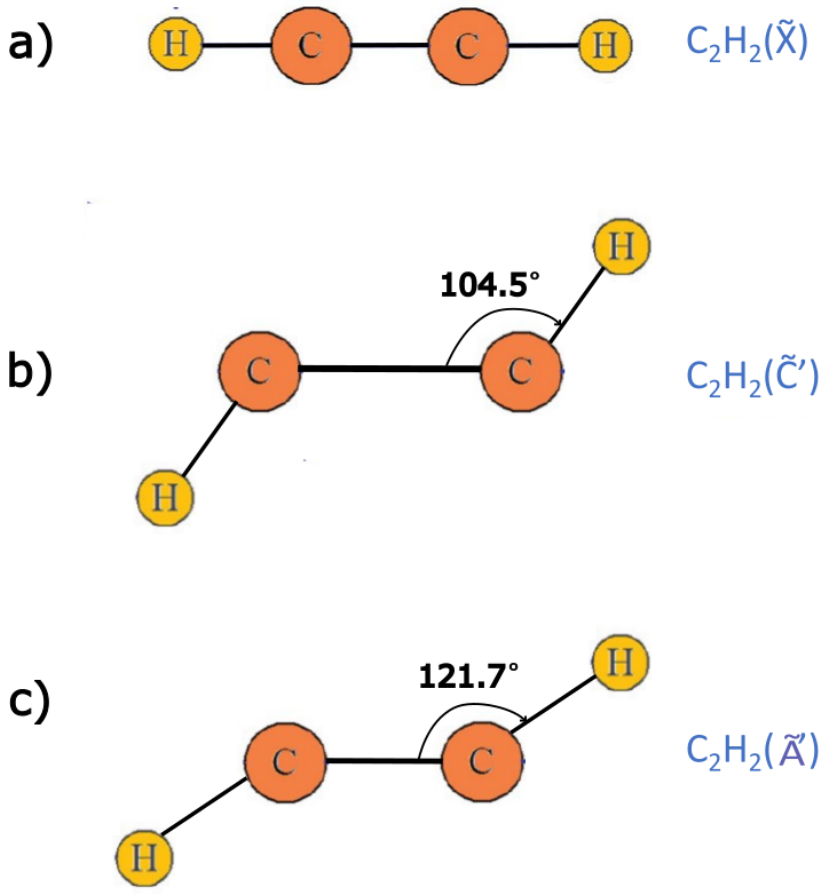

FIGURE 2.10: Schematic representation of the a) ground state $\tilde{X}$, b) $\tilde{C}'$ and c) $\tilde{A}$ excited valence states of acetylene. The apex angles were predicted theoretically by Laurelle and co-workers [16].

In terms of geometry, the excited state $\tilde{C}'^1A_g$ adopts a trans-bend structure as shown on Figure 2.10 and belongs to the point group C_{2h} [39]. In particular, Lundberg [38] calculated the rotational constants of the molecule by studying the long progression in the C-C stretch, the trans-bending vibration, and a combination of

them in his spectra due to the geometry change of the molecule in the transition from $\tilde{A}^1A_u$ to the $\tilde{C'}^1A_g$ state. The apex angle between C-C-H changes from 120° to 103° while R_{CC} and R_{CH} were found to be equal to 1.652 and 1.143 respectively. The theoretical study performed by Laurelle and co-workers [16] revealed good agreement with the experimental values. Moreover, Lundberg unraveled the pre-dissociating character of the $\tilde{C'}^1A_g$ Valence state which is labeled as Herzberg's type II pre-dissociation [26] as the molecule is led to fragmentation through additional vibrational excitation [38]. As far as the $\tilde{A}^1A_u$ excited valence state is concerned, Ingold, King [36] and Innes [41] studied extensively the absorption spectra of acetylene in the spectral range $210 - 240\ nm$ and found that the state possesses a trans-bend planar geometry (see Figure 2.10c) compared to the linear structure of the $\tilde{X}^1\Sigma_g^+$ ground state leading to a long-progression spectrum in the excitation spectra to this state from the ground state. The intermolecular distances were found to be in good agreement with calculations made by Laurelle [16].

Chapter 3

Experimental setup

The main purpose of this chapter is to describe the experimental setup that was used throughout the study of the laser induced photooxidation of acetylene. The study was carried out using 2 experimental setups. The first setup was used to record the multiphoton ionization spectra of acetylene between 280 and 325 nm, while the second setup was used to study the time evolution of the absorption spectra of glyoxal which was also the case in the work done by P. Kalaitzis and co-workers [4]. However, in the current study of the photooxidation reaction, several experimental upgrades have been added, such as the inclusion of a Frequency Convertion Unit, the increased range of the study and a more controlled environment of the pulse energy. Before we discuss the setups, let's briefly discuss the laser dyes, as well as how the second harmonic is produced and isolated from the fundamental and how it reaches the experiment. Overall, this chapter will be divided into 3 sections as:

- A brief discussion about the laser dye compounds, the pumping fundamental beam and the Frequency Convertion Unit (FCU) responsible for the second harmonic generation.
- Multiphoton ionization setup and acquisition process.
- Photooxidation setup and acquisition process.

3.1 Laser dyes - FCU

Dye lasers use certain compounds, known as laser dyes, as gain media and produce a narrow and tunable laser light [42]. Laser dyes are organic compounds with unique optical properties designed to efficiently absorb light energy and emit it as coherent laser light [42]. These dyes are typically dissolved in a suitable solvent to form a dye solution. Common examples of laser dyes include rhodamines, coumarins, fluoresceins, and perylene derivatives [43]. Each dye has its own characteristic absorption and emission spectrum which allow tunability over a wide range of wavelengths [42]. The choice of dye affects the output wavelength and properties of the dye laser, making it an essential component in tailoring the laser to specific applications, such as spectroscopy, biomedical research, and materials processing.

The versatility of laser dyes, combined with the ability to fine-tune the output wavelength, makes dye lasers valuable tools in a variety of scientific and technological fields [44].

A dye laser is a type of laser that utilizes the optical properties of some organic molecules containing double and triple bonds as the gain medium in order to produce laser light which has a narrow spectral range and is tunable. In order to produce the tunable radiation, a high-intensity pulse at 532 or 355 nm (originating from an Nd:YAG Laser at 1064 nm) excites the dye molecules which produces coherent laser light as well as incoherent radiation (Amplified Spontaneous Emission (ASE)). The coherent laser light gets trapped in an optical resonator which acts as an amplifier by reflecting the light back and forth inside the resonator and thus stimulating more molecules. The wavelength that comes into resonance and is amplified inside the cavity is selected with the help of a grating.

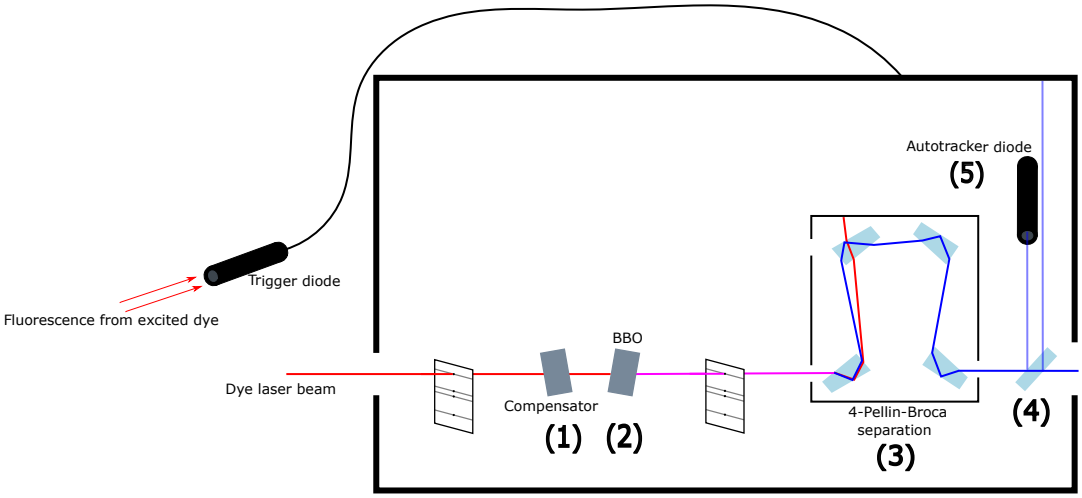

FIGURE 3.1: Schematic illustration of the Frequency Conversion Unit (FCU).

For the production of the fundamental beam in our experiment, we use a tunable Lambda Physic Scanmate laser utilizing an Nd-YAG laser source. The Nd-YAG beam at 1054 nm is frequency doubled with a BBO crystal and then splits into 3 parts. The oscillator, pre-Amp and Amp beams. The first 2 beams are driven to the quvette containing the dye compound (albeit in a different concentration) and with the help of an optical cavity containing a reflecting mirror and a grating (for tuning purposes), the beam gets pre-Amplified. The pre-Amplified beam reaches a second quvette (which is already pumped by the Amplifier beam) which contains the same dye compound and by stimulated emission the final fundamental beam is further amplified.

The laser dyes we worked with are: DCM, LC6100 and LC5900 covering the ranges $606 - 650\ nm$, $584 - 614\ nm$ and $558 - 579\ nm$ respectively. The absorption of these dye compounds as well as their specifications are shown in Appendix B. In order to have a better insight on the distribution of the intensity throughout the

whole spectral range the dye covers, we record the dye profile of each dye as shown in Figure 3.2 with the setup shown on Figure 3.3.

In order to record the dye profiles, a photodiode was placed in front of the laser beam which is passed through a diverging lens to increase the beam radius reducing the likelihood of photodiode damage. Then, the signal is inserted to a boxcar and analog-to-digital converter system and is recorded using a computer and specialized LabVIEW software[1].

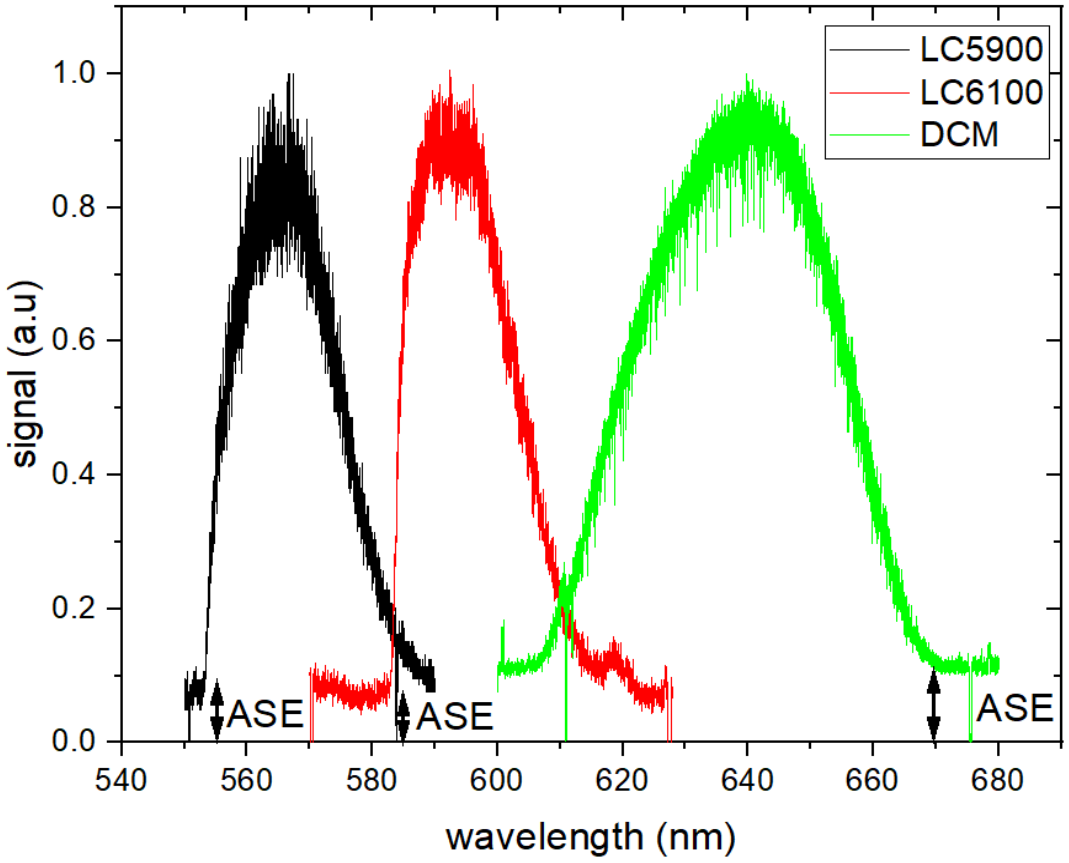

FIGURE 3.2: Normalized dye profile of the dyes used (DCM, LC6100, LC5900).

Now, for the production of the second harmonic, we use a BBO crystal as the non-linear material where 2 photons of the same wavelength interact with it and produce a 3^{rd} photon with twice the energy and half the wavelength of the 1^{st}. The BBO crystal is located inside the Frequency Conversion Unit (and hence FCU) which has 2 majors roles. The ionization experiment exploits the scanning ability of the Autotracker Unit (AT) while the photooxidation experiment uses the FCU just to select the wavelength by turning the BBO crystal semi-automatically. A complete description of the FCU can be found in Appendix A and the schematic illustration is shown in Figure 3.1. In our experiments, we require tunable radiation in the UV range. This is achieved by propagating the dye laser beam into the Radiant-Dyes Frequency Conversion Unit which incorporates an AutoTracker (AT) unit. In Figure 3.1 we show the optical layout of the FCU unit used for the production of the UV

[1]The LabVIEW software was developed by the group o S. Cohen.

radiation. The elements it incorporates are: (1) a compensator, (2) a frequency doubling crystal, (3) a set of four Pellin-Broca prisms, (4) a beam splitter , (5) a photodiode, and incorporates an autotracker (AT) unit. The complete description regarding the operation of the AT can be found in Appendix A.

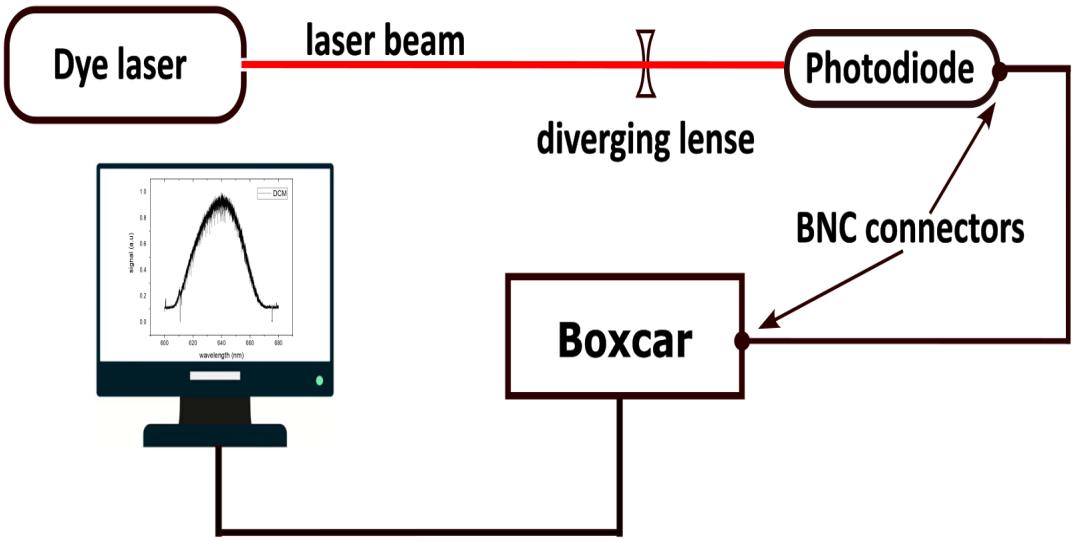

FIGURE 3.3: Schematic illustration of the setup used to record the dye profile.

The tunable radiation passes through a compensator-BBO crystal system to correct the path of the beam so that the harmonic and the fundamental beam come out parallel to the original beam as shown in Figure 3.1. When changing the fundamental wavelength, both compensator and BBO crystals have to turn in different directions in order to minimize deflection which is done with the help of the AT circuit. This BBO crystal is designed to produce second harmonics in the range of 220-320 nm with efficiency up to 25%. Acorrding to manufacturer's test, 5 mJ of input pulse energy produce a second harmonic of 1.6 mJ pulse energy and these specifications are verified in our experiment. After passing through the BBO crystal, both fundamental and second harmonic propagate in parallel and enter an assembly of 4-Pellin Broca prisms. Due to the fact that the prisms have different refractive indices for each wavelength, the two-color beam splits and eventually the fundamental beam gets blocked. As a result, only the second harmonic comes out of the Pellin Broca system making it an efficient way to filter out the radiation that is not needed for the experiment. Finally the beam reaches a beam splitter which splits it into 2 parts, a small one (order of 4%) which is fed to the autotracker diode, while the other is used at the experiment.

3.2 Multi-photon ionization setup

Multi-photon ionization can be used to detect and study the excited states (Rydberg or Valence) involved in our experiment. Excitation to a Rydberg state can be performed using either one or more photons, depending on the energy of the state, the

photon energy and the selection rules. For a given number of photons, a transition can be allowed or forbidden. In our experiment, acetylene ionization proceeds via a 2+1 Resonance Enhanced Multiphoton Ionization (REMPI) scheme. In these experiments, only the relatively long-lived Rydberg states can be observed. Rydberg states that dissociate rapidly, say a few tens of fs, cannot be observed using ns lasers and REMPI and require specialized techniques.

In order to obtain the multi-photon ionization spectra we used the setup shown in Figure 3.4. Similar to the photooxidation experiment, the fundamental dye beam

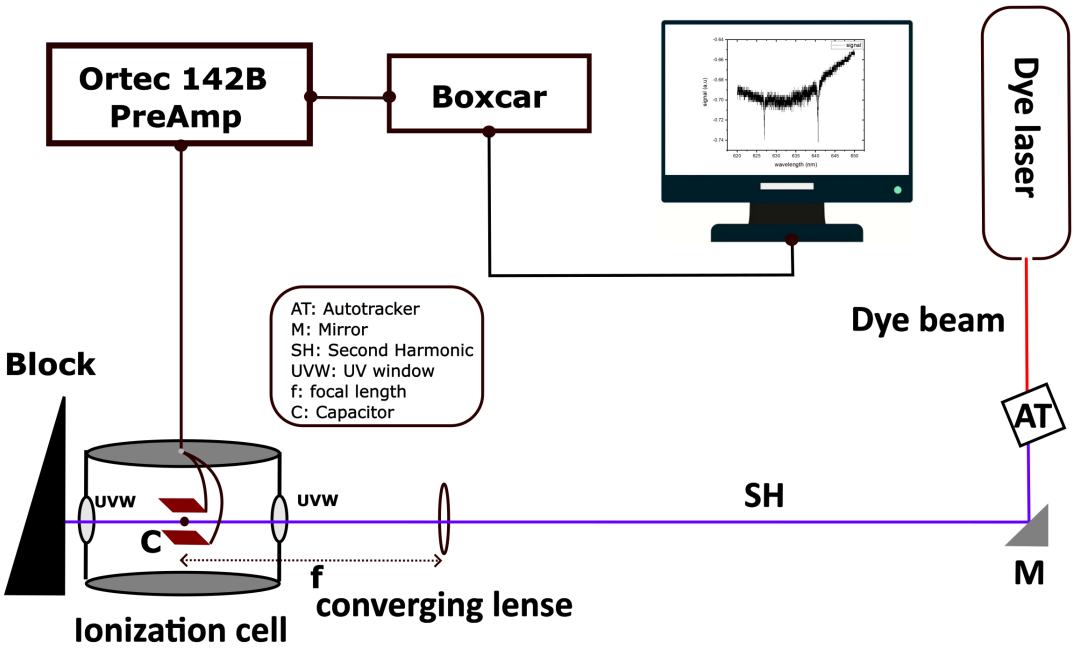

FIGURE 3.4: Schematic illustration of the multi-photon ionization experimental scheme.

is subject to frequency doubling. The second harmonic is focused using a 5 cm focal length converging lens between 2 metallic plates (distance between the metallic plates is about 1.5 cm) of a capacitor placed inside the ionization cell. The pulse energy of the laser beam varied between the runs from 0.8 mJ to 1.4 mJ. This variation is due to the inability of the AT to maintain constant intensity as it follows the dye profile while scanning. When ionization occurs, electrons, which are no longer bound to the acetylene molecule, accelerate due to BIAS DC voltage applied between the metallic plates of the capacitor and hit them, creating a small voltage peak which is amplified in Ortec's 142B PreAmp [45] as shown in Figure 3.5. Then, the signal is recorded in a computer using the same LabVIEW program after getting digitized by Boxcar-AtoD system.

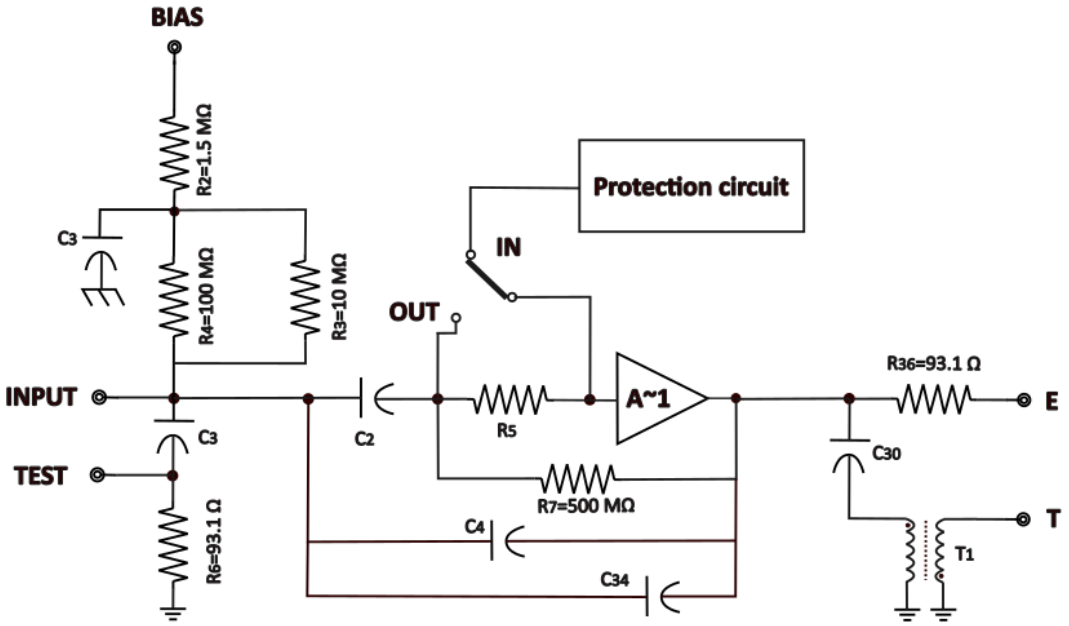

FIGURE 3.5: Schematic illustration of the circuit inside Ortec 142B (pre-Amplifier) [45].

To briefly describe the circuit we must first refer to Ortec's manual [45] for the indications BIAS, INPUT, TEST, E and T. BIAS accepts the external DC voltage from a power supply while INPUT accepts input signals from the charged-particle detector [45]. The Test indication is used for instrument calibration with input voltage pulses from a pulse generator of $R_{in} = 93\Omega$, E stands for energy measurements while T stands for timing applications. There is also a protection circuit installed, to protect the input Field Effect Transistor (FET) from large transient voltages which are capable of damaging the transistor. The applied bias is furnished to the detector with the help of resistors R_2 and R_3 [45]. If there is a noticeable current leakage in the detector then, a resistor R_3 must be inserted in parallel with R_4 [45].

In our experiment, the BIAS input that was used did not exceed 250 V ranging from 40 V to 250 V. Regarding the multi-photon ionization spectra, the cell contained only acetylene in various pressures depending on the measurement. The starting pressure (pressure at the beginning of the experiment) varied in the range $1 - 3$ $Torr$ depending on the scan. The velocity of the wavelength scanning was 0.01 nm/sec and the scanning region that was studied lied between $558 - 650$ nm (and hence 0.005 nm/sec in the second harmonic). Due to the small step, which led to an increased duration of the scan, the pressure inside the ionization cell was constantly increasing. The scanning velocity cannot increase much otherwise the AT will not work. For this reason, it has often been necessary to break the scan into smaller parts and renew the sample, in order to get the best possible result. In a fixed BIAS input, electrons bump into the metallic plates more often in low pressure than in high pressure due the decrease in the mean free path of the particles inside the cell. As collisions between electrons and molecules become more often, less electrons hit the plates.

3.3 Photooxidation setup

In order to study the acetylene photooxidation reaction, we used an experimental setup consisting of the following elements:

- a Frequency Conversion Unit
- an SL201 L/M broadband source
- UV absorbing filters
- a $\times 1/3$ telescope
- a hollow parabolic mirror
- a 1 m fused silica cell with a diameter of 1.1 mm
- 4 lenses
- an Andor Shamrock SR-301-iB spectrometer.

The experimental setup is shown on Figure 3.6. The second harmonic propagates

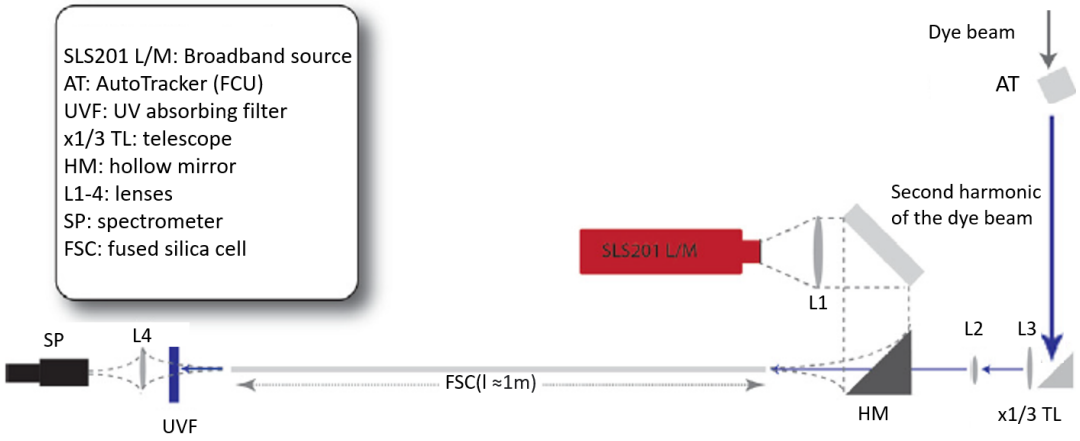

FIGURE 3.6: Experimental setup for the study of glyoxal production [4].

into the fused silica cell after passing through an ($\times 1/3$) optical telescope and through the hole of a parabolic mirror. The light coming from the broadband light source (SLS201 L/M) is focused from the parabolic mirror into the fused silica cell. This light is used to record the absorption spectra of the products within the fused silica cell. After the fused silica cell, there is a lense (L4) which focuses the light on the input of a spectrometer (Andor Shamrock SR-301-iB, utilizing a Newton EM CCD camera [46]). UV filters (UVF) are used to block the laser incoming radiation. Within the cell, the acetylene and oxygen gases are inserted (Air Liquide, purity > 99.6%) and the mixing ratio was 1:1 throughout the whole experiment (400 Torr O_2 and 400 Torr C_2H_2).

As mentioned earlier, the experiment was performed using tunable radiation in the range of 279-325 nm generated by frequency doubling of the tunable dye laser

radiation. Our first observation was that the glyoxal production increases as the wavelength of the second harmonic decreases. Glyoxal has a lifetime of a few minutes and after it decays, various compounds are produced that stick to the walls of the cell and change the color of the cell. Thus, we worked at low intensities to keep the cell as clean as possible. The pulse energy of the frequency doubled beam right after the pumped fused silica cell varied from 0.28 mJ to 0.7 mJ depending on the measurement. For a better mixing efficiency, the mixture was prepared in a pre-chamber before entering the fused silica cell.

The spectrometer used in the experiment, it is an Andor Shamrock SR-301-iB [46] spectrometer, with a motorized slit which is controlled with the Andor Solis for Spectroscopy software [47]. In our case, the slit was set at 100 μm (optimal condition for our experiment), the grating lines were set to 150 l/mm and the blaze to 500 nm. A Newton EM CCD camera is used by the spectrometer in order to record the spectra. A charged-coupled device (CCD) is a small light sensitive circuit which converts light signal to electron signal (charge). Light impacting on a pixel leads to the production of electric charge which is proportional to the intensity of the light captured by that particular pixel. Figure 3.7 shows the panel of the Andor SOLIS for Spectroscopy software [47], where one can see a spectrum of the SLS201 L/M lamp. In this panel, we can also see the settings used in our experiment inside red rectangles. As shown in figure 3.7, the CCD camera operated at $-30\ ^{\circ}C$ for high signal to noise ratio (SNR). In the following sub-section, we will provide a detailed description on how the data were extracted and manipulated.

3.3.1 Data acquisition

In this sub-section, we will discuss the extraction and manipulation process of the data produced in our photooxidation experiment. Firstly, we will discuss the step by step acquisition process and then get into details about the spectrometer.

A gas mixture consisting of 400 Torr of Acetylene and 400 Torr of molecular Oxygen are mixed in a pre-chamber before entering the cell. The measurement starts at time $t = 0$ sec. We record the spectra every 2.125 sec while the laser enters the cell at time $t \approx 8.5$ sec, and using a Wolphram Mathematica [48] software[2] we extract the absorption of glyoxal over time.

For our measurements, we use the Andor Shamrock SR-301-iB spectrometer in the 'Kinetic Measurement' mode. In this mode, a series of spectra are recorded at equal time intervals. The exposure time and the number of accumulations were set to 0.085 sec and 25 respectively. Due to the nature of each measurement (reactivity varies in function with the wavelength of the incoming radiation), the kinetic cycle also varied. Figure 3.8 shows the settings used in our measurements. After extracting the spectra, we use a Wolphram Mathematica [48] software to calculate the area of one of glyoxal's absorption peak in each kinetic cycle and produce the absorption

[2]The Wolphram Mathematica software was developed by P. Kalaitzis [4]

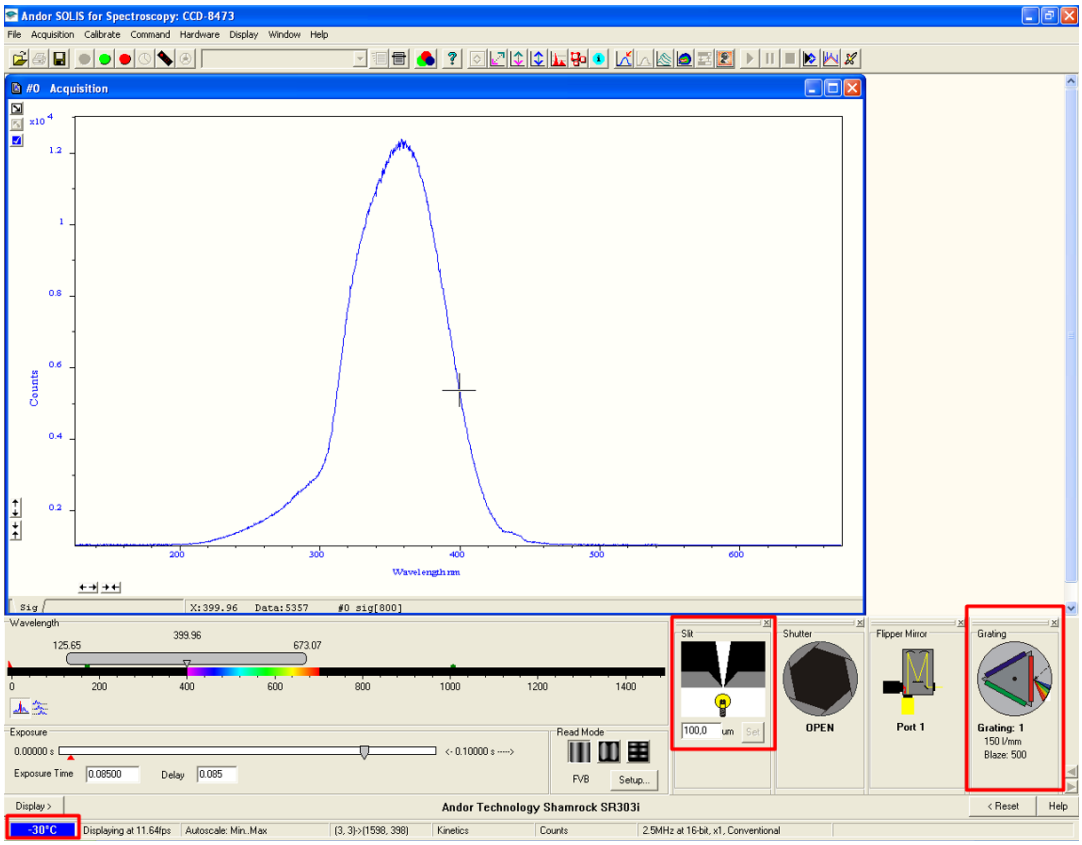

FIGURE 3.7: Panel of the Andor SOLIS for Spectroscopy software [47], showing the spectrum of the SLS201 L/M lamp. We can see the spectrometer settings used in our experiments in red rectangles.

of glyoxal as a function of time, showcasing quantitavely the time evolution of glyoxal production. In greater detail, the software divides each spectrum by the first spectrum where the amount of glyoxal is zero as the reaction has not yet started. Figure 3.9a shows the time evolution of the glyoxal absorption. We see that in this particular example, the absorption at time $t = 22.5\ sec$ is about 7%. At this point, we should mention that, time $t = 0\ sec$ was defined as the moment when the laser starts interacting with the gas mixture, while in terms of measurement, the actual time when the gas mixture starts interacting with the laser is about $t = 8.5\ sec$.

The area under the glyoxal main peak around 285 nm was calculated by integrating the spectral region between 284 and 290 nm as shown on Figure 3.9b. The time dependence of this signal, for radiation at 284 nm is shown in Figure 3.10. Laser initiates the reaction at $t \approx 8.5\ sec$ and glyoxal increases. In order to extract the reaction rate

$$\kappa = \frac{1}{\tau} \tag{3.1}$$

with κ being reaction rate τ the reaction time, we fit our data to the following formula:

$$A(t) = Ae^{(t-t_0)/\tau} + B \tag{3.2}$$

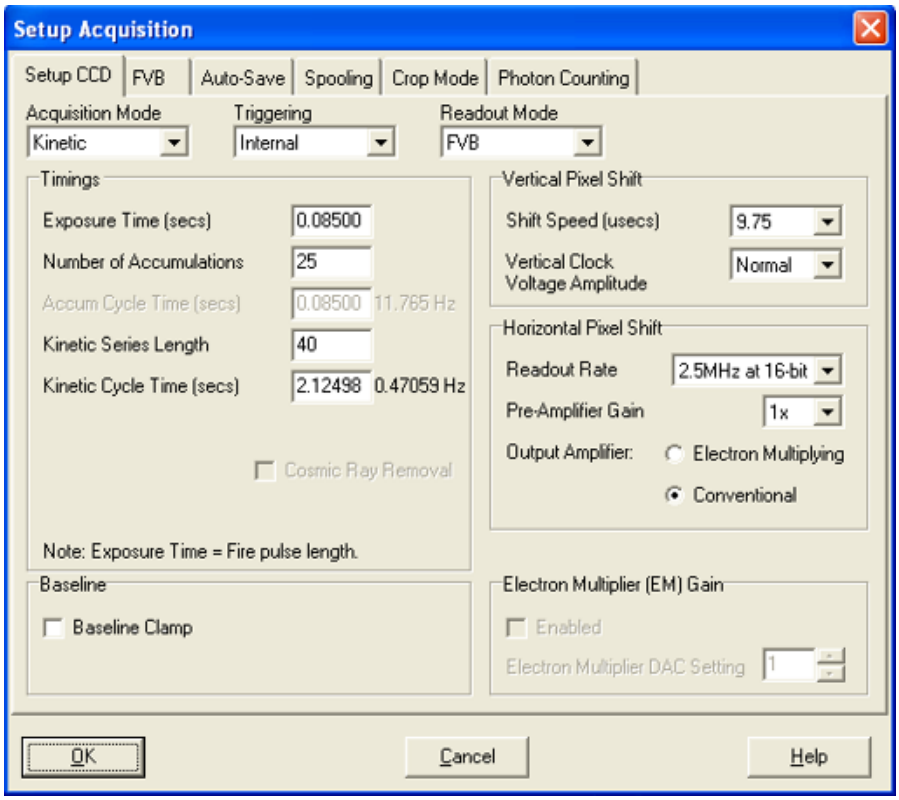

FIGURE 3.8: Spectrometer settings used in the Kinetic Measurements.

with t_0 being the start time of the reaction, $A(t)$ being the time dependent absorption, A, B being free fit parameters related to the absorption and τ being the characteristic time constant to be extracted [4]. Such a fit is shown in Figure 3.10 for laser radiation at 284 nm.

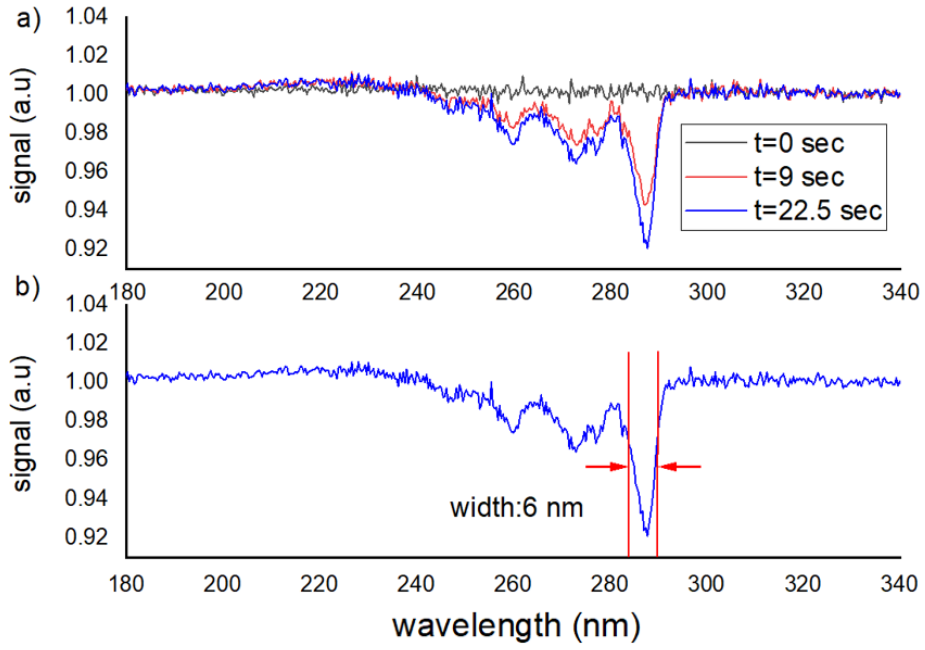

FIGURE 3.9: a) Time evolution of glyoxal absorption. b) Spectral window of integration utilized by the Wolphram Mathematica software.

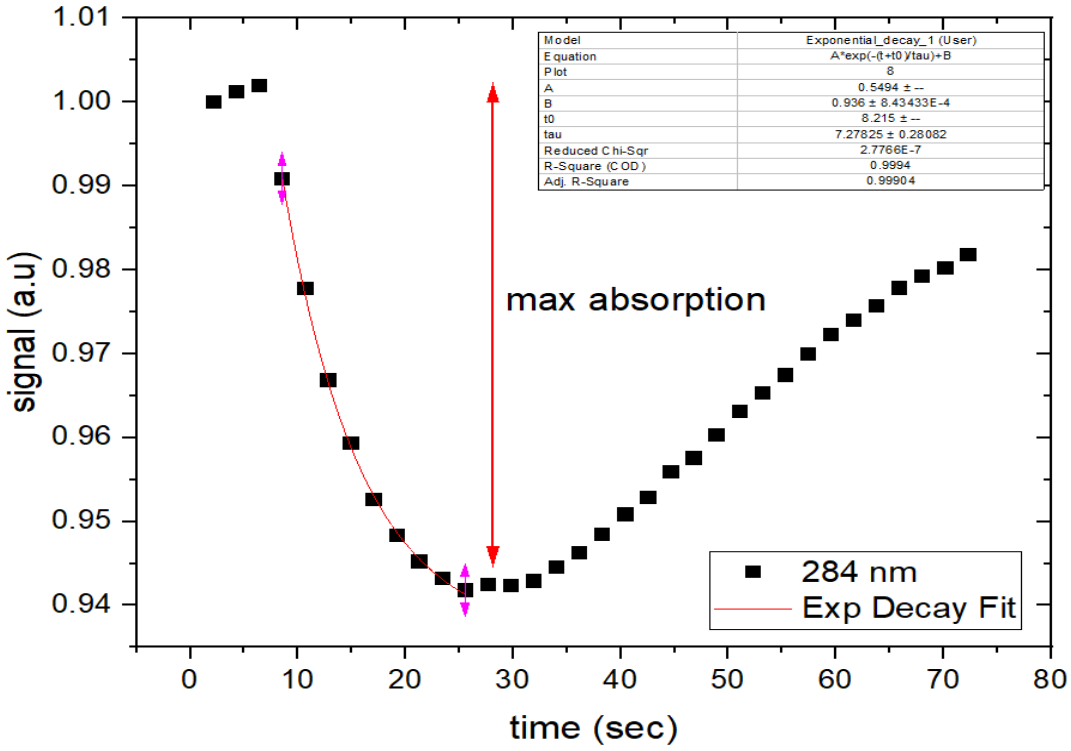

FIGURE 3.10: Glyoxal production as a function of time for 284 *nm* laser radiation along with the exponential fit for the extraction of τ.

Chapter 4

Results - Discussion

In this chapter, we are going to present and manipulate the data derived from our experiments as well as discuss our results. This chapter will be divided into 4 sections:

- Results and discussion of multiphoton ionization experiment.
- Results and discussion of photooxidation experiment. [4].
- Discussion on the mechanisms of photooxidation observed in our experiment.

4.1 Multiphoton ionization - Results

4.1.1 DCM (310-325 nm)

Starting from the Table (table 2) obtained from Fabrice Laruelle et al. [16] we determine the excited electronic states of the acetylene molecule.

According to Figure 4.1b the valence state $\tilde{C}'^1A_g$ is within reach via a 2 photon absorption process and in order to obtain the ionization signal of this electronic state, an extra photon must be absorbed. Figure 4.2 shows the uncalibrated multiphoton ionization spectra around the $\tilde{C}'^1A_g$ line. Using the $\tilde{C}'^1A_g$ line we can estimate the experimental error (shift) in the laser calibration. This shift was found to be 0.91 nm compared to previous experimental works [38], [55] and is corrected in all measurements hereafter. Figure 4.3 shows the multiphoton ionization spectra of acetylene in the entire spectral region of the DCM's laser second harmonic ($310 - 325\ nm$). In this range, another line is observed centered at 314.4 nm that needs identification.

Before we try to identify this new line, let's take a moment to discuss the shape of the signal shown in Figure 4.3 as well as the factors that affect the signal. The ionization signal consists of the resonant signal and a broad background. Both signal and background are proportional to the pulse energy. Since the laser output is increased around 630 nm (fundamental wavelength) and decreased at 650 nm (see laser dye profiles Figure 4.9), the background minimizes around 620 and 625 nm and peaks around 635 nm. Although the pulse energy varied during the scan, both in the beginning and at the end it was measured to 1.1 mJ. Moreover, the BIAS voltage applied to the metallic plates of the capacitor was 120 V. The last factor that

a)

type	label	main orbital excitation	Fabrice Laruelle's work or otherwise indicated $R_{CC}/R_{CH}/\alpha$	adiabatic T_e	exptl T_0
GS	$\tilde{X}\ ^1\Sigma_g^+$		1.210/1.065/180.0	0	0
V	$\tilde{A}\ ^1A_u$	$1\pi_g$	1.380/1.097/121.7[d]	5.24[d] (5.26)[d]	5.23[e]
V	$\tilde{B}\ ^1B_u$	$1\pi_g$	1.337/1.077/148.5[d]	6.78[d] (6.78)[d]	6.71[f]
V	$2\ ^1A_u$	$1\pi_g$	1.327/1.065/171.5[d]	6.91[d] (6.90)[d]	7.2[g]
V	$\tilde{C}'\ ^1A_g$	$(1\pi_g)^2$	1.621/1.096/104.5[h]	7.53	7.72[i]
R	$\tilde{C}\ ^1\Pi_u$	$3s\sigma_g$	1.254/1.073/180.0[d]	8.174	8.16[j]
R	$3p\ ^1\Pi_g$	$3p\sigma_u$	1.266/1.112/180.0	8.433	
R	$3p\ ^1\Delta_g$	$3p\pi_u$	1.252/1.077/180.0	8.998	9.01[k]
R	$3p\ ^1\Sigma_g^-$	$3p\pi_u$	1.252/1.078/180.0	9.055	
R	$3p\ ^1\Sigma_g^+$	$3p\pi_u$	1.252/1.079/180.0	9.157	9.21[k]
R	$\tilde{D}\ ^1\Pi_u$	$3d\sigma_g$	1.254/1.113/180.0[d]	9.374	9.24[l]
V	$\tilde{E}\ ^1B_u$	$1\pi_g$	1.276/1.102/161.2[d]	9.36 (9.39)	9.25[l]
R	$\tilde{F}\ ^1\Sigma_u^+$	$3d\pi_g$	1.262/1.081/180.0	9.532	9.27[j]
R	$\tilde{F}'\ ^1\Phi_u$	$3d\delta_g$	1.254/1.078/180.0	9.886	9.91[m]
R	$\tilde{H}\ ^1\Pi_u$	$3d\delta_g$	1.254/1.078/180.0	9.903	9.98[j]
R	$\tilde{G}\ ^1\Pi_u$	$4s\sigma_g$	1.254/1.078/180.0	9.922	9.93[j]
R	$\tilde{H}'\ ^1\Delta_u$	$3d\pi_g$	1.259/1.080/180.0	9.975	10.0[n]
R	$^1\Sigma_u^-$	$3d\pi_g$	1.259/1.079/180.0	9.974	
R	$4p\ ^1\Pi_g$	$4p\sigma_u$	1.262/1.095/180.0	10.014	
R	$4p\ ^1\Delta_g$	$4p\pi_u$	1.254/1.077/180.0	10.175	10.24[k,o]
R	$4p\ ^1\Sigma_g^-$	$4p\pi_u$	1.254/1.077/180.0	10.193	
R	$4p\ ^1\Sigma_g^+$	$4p\pi_u$	1.255/1.078/180.0	10.227	10.29[o]
R	$5p\ ^1\Pi_g$	$5p\sigma_u$	1.254/1.080/180.0	10.613	
R	$5p\ ^1\Delta_g$	$5p\pi_u$	1.253/1.075/180.0	10.667	10.71[o]
R	$5p\ ^1\Sigma_g^-$	$5p\pi_u$	1.253/1.075/180.0	10.674	
R	$5p\ ^1\Sigma_g^+$	$5p\pi_u$	1.255/1.075/180.0	10.687	10.73[o]
cation	$\tilde{X}\ ^2\Pi_u$		1.247/1.075/180.0[p]	11.38[p]	10.401[q]

b)

2+1 MPI

fundamental (nm)	SHG wavelength (nm)	Dye
642.48	321.24	DCM
607.84	303.92 (2+1) forb	DCM, LC6100
588.38	294.19	LC6100
550.5	275.25	
547.76	273.88	
541.66	270.83	
536.8	268.4 (2+1) forb	
536.22	268.11 (2+1) forb	
535.06	267.53 (2+1) forb	
500.5	250.25 (2+1) forb	
497	248.5 (2+1) forb	
499	249.5 (2+1) forb	
496	248 (2+1) forb	
496	248 (2+1) forb	
495.30	247.65	
484.36	242.18	
486.60	243.30	
482.02	241.01	
467.36	233.68	
463.12	231.56	
464.68	232.34	
462.26	231.13	

FIGURE 4.1: a) Results from [16] determining bond lengths and energy of each excited state. b) Calculation of 2+1 ionization energies and corresponding wavelengths. [a] All calculations are performed at the VTZ+Ryd/CMRCI level of theory [16]. T_e values in parentheses are calculated with an AVQZ basis set at VTZ optimized geometries [16]. [b] From Zyubin and Mebel [49]. The two levels of theory are using different basis sets. [c] From Malsch et al [50]. Values in parentheses correspond to optimized CASSCF geometries [16]. [d] From Blanchet et al [51]. [e] From Pujii [40]. [f] From Foo and Innes [41]. [g] From Dressler and Allan [52]. [h] From Lievin [39]. [i] From Lundberg et al [38]. [j] From Herman and Colin [53]. [k] From Ashfold et al [54]. [l] From Herman and Colin [55]. [m] From Ashfold et al [56]. [n] From Fillion et al [57]. [o] From Tsuji et al. [58]. [p] From Boye´-Pe´ronne et al [59]. [q] From Ruppert and Merkt [60].

affects our signal is pressure. The study shown in Figure 4.3 was performed with a 0.0025 nm/sec scanning velocity making the measurement last about 100 minutes. During the measurement, the pressure increased linearly as shown in Figure 4.4. The increasing pressure lowers the signal as the mean free path (in our case, the mean free path is around 3 mm when the cell is filled with 1.5 *Torr* of Acetylene and the distance between the metallic plates is around 1.5 cm) between molecules decreases which means that more collisions occur inside the cell and thus less electrons reach the capacitor. In our experiment, the increase in pressure is explained by the fact that atmospheric air enters the cell.

In order to be sure that the spectral lines that we observe indeed come from Acetylene ionization, we perform the following tests:

- fill the cell with molecular Nitrogen and Oxygen.
- pump the cell multiple times both before and after a measurement and search for differences.

- perform the same measurement the same measurement at different times of the day

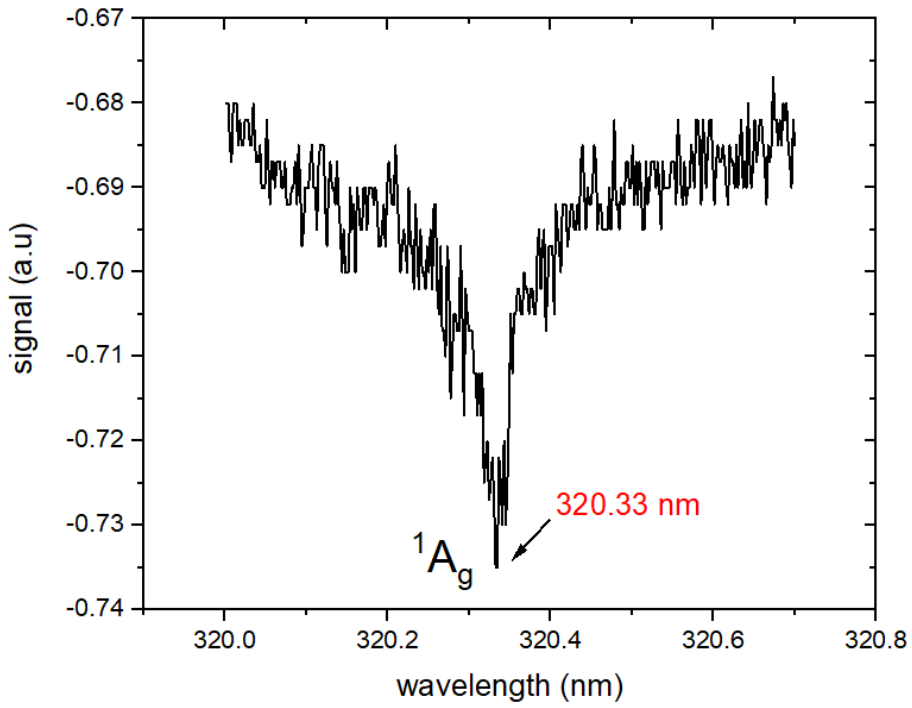

FIGURE 4.2: Uncalibrated 2+1 Multiphoton ionization spectra around the $\tilde{C}'^1A_g$ valence electronic state.

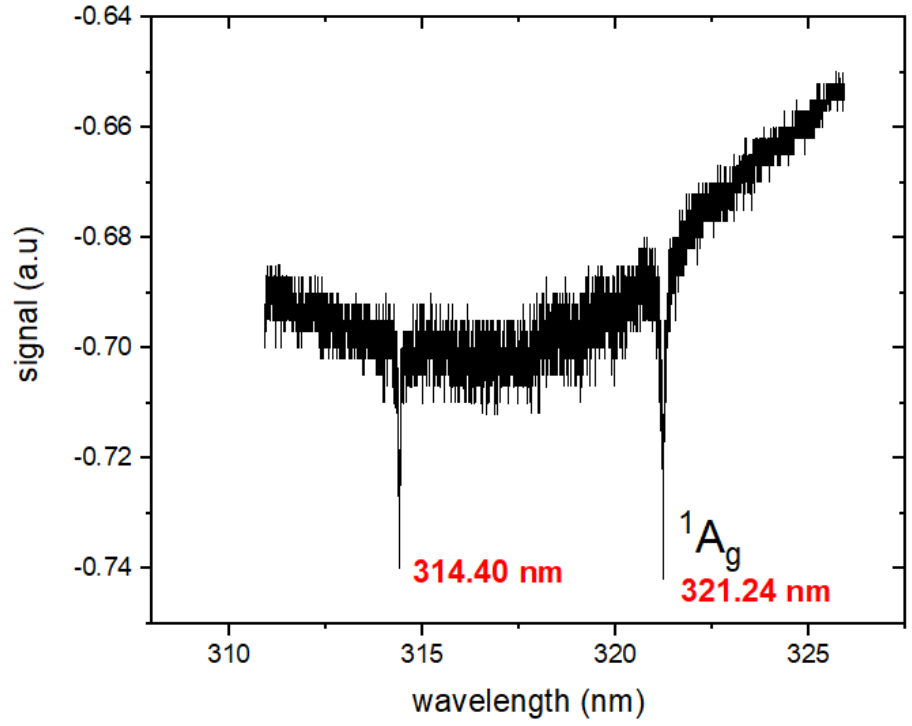

FIGURE 4.3: Calibrated 2+1 multiphoton ionization spectra of acetylene regarding the second harmonic of DCM dye laser.

The cell was filled with molecular Nitrogen and Oxygen (after pumping the cell for a day), and a small scan around $\tilde{C}'\tilde{C}'^{1}A_g$ was performed but revealed no evidence of the line. The scan was performed multiple times and the result was the same, no signal. But when we filled the chamber with acetylene and then pumped it in order to make the same measurement with atmospheric air, we saw some evidence of the line which is attributed to the fact that acetylene stack to the walls of the cell (Figure 4.5).

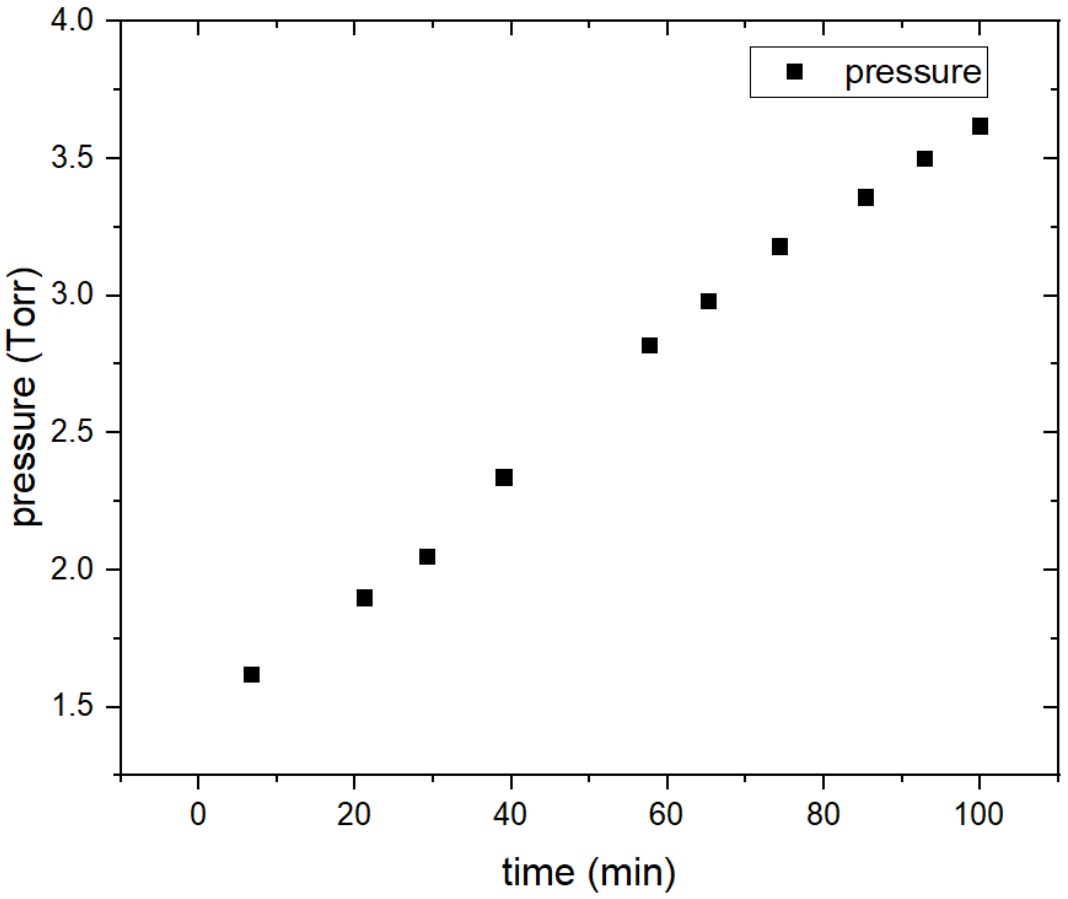

FIGURE 4.4: Pressure over time during DCM dye scan. The initial and final output pulse energy was 1.1 mJ.

Now, for the line around 314.40 nm, the same procedure was applied and the results are shown in Figure 4.6. Both scanning velocity and pressure varied between the scans but the pulse energy remained unchanged at 1.1 mJ. The peak is present in all of our measurements even though the cell was not filled with acetylene. On Figure 4.7, we show the first and the last measurement of the day. The first measurement was performed before filling the cell with acetylene (we pumped the cell for a day) while the last was made after pumping the cell multiple times and using only atmospheric air. In the first measurement we observe no sign of the unknown line while in the last measurement there is clear evidence of the line demonstrating that acetylene sticks to the walls of the cell. Both measurements were taken with

pure atmospheric air but between the measurements acetylene was present inside the ionization cell.

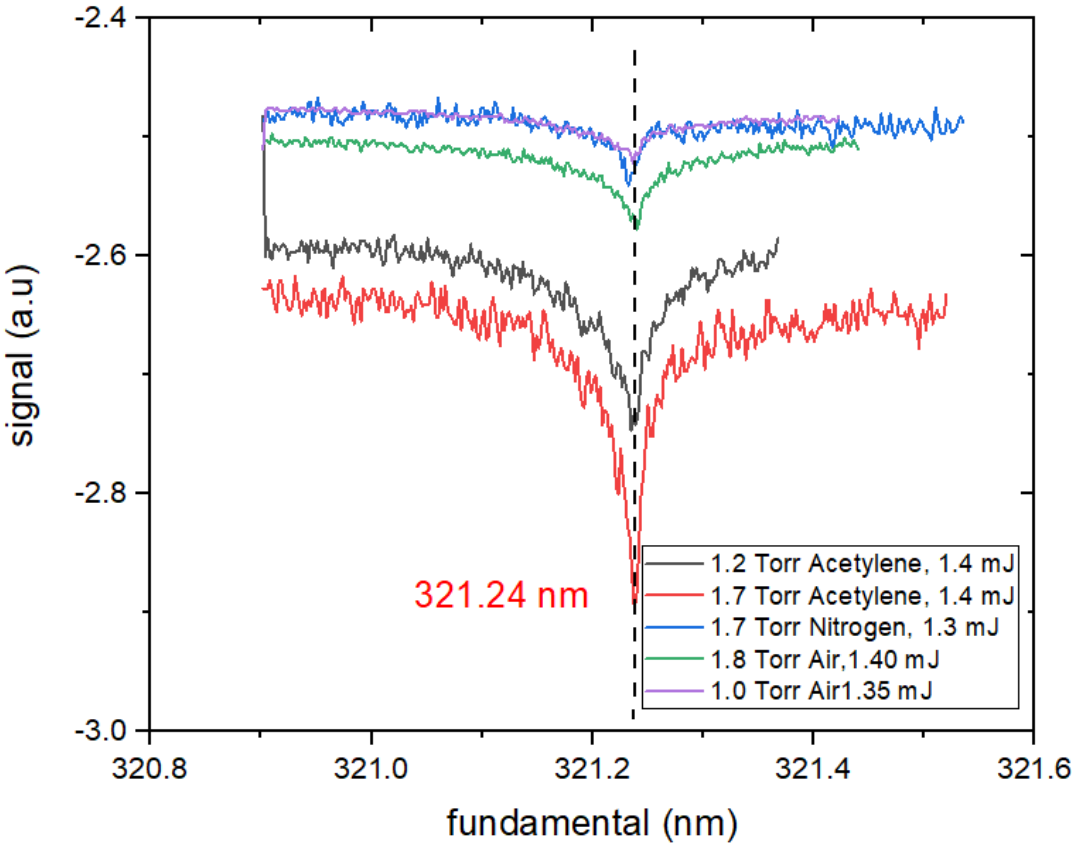

FIGURE 4.5: Intermediate scans with or without acetylene. Nitrogen and Air measurements were performed after the acetylene measurements.

According to Fabrice Laurell and James K. Lundberg's work [16], [38], the electronic state $\tilde{C}'^1A_g$ belongs to the trans-bent C_{2v} point group with bond distances and apex angle that are shown in Figure 4.1. James K. Lundberg et al. [38] found experimental evidence of the same line centered at 314.4 nm by using Ultraviolet-Optical-Double-Resonance (UVODR) [38] spectra via individually selected rotational - vibrational intermediate levels in the ^1A_u state. Lundberg et al attribute this line to a vibrational normal mode v_3 of the trans-bent C_{2v} acetylene with energy 1303 cm^{-1} (theoretical value 1386 cm^{-1} [39]), while in our case, we observe this line at around 1354 cm^{-1}. It is also stated that Valence state $\tilde{C}'^1A_g$ assisted by a vibration v_3 is a partially dissociating state with a lifetime on the order of a few hundreds of ps [38]. By performing a fit with Lorentzian type functions we calculate the width at the FWHM and end up with a lifetime of 0.6 ps. This type of pre-dissociation occurring after vibrational excitation is called Type II predissociation, in contrast to Type I pre-dissociation where only the electronic excitation leads to pre-dissociation via conical intersection crossing [26]. Type II dissociation is about 10 times slower that Type I dissociation [26].

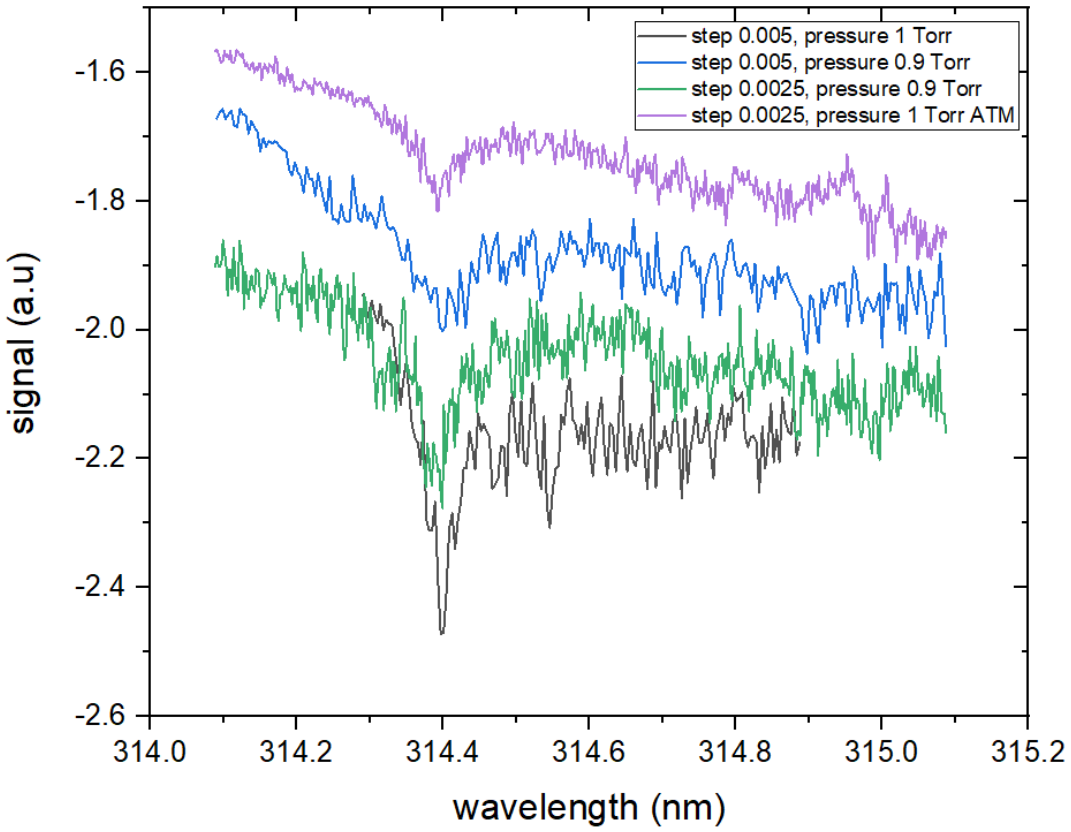

FIGURE 4.6: Same measurement under similar conditions. The cell was filled with acetylene unless otherwise indicated. Step: scanning velocity in nm/sec

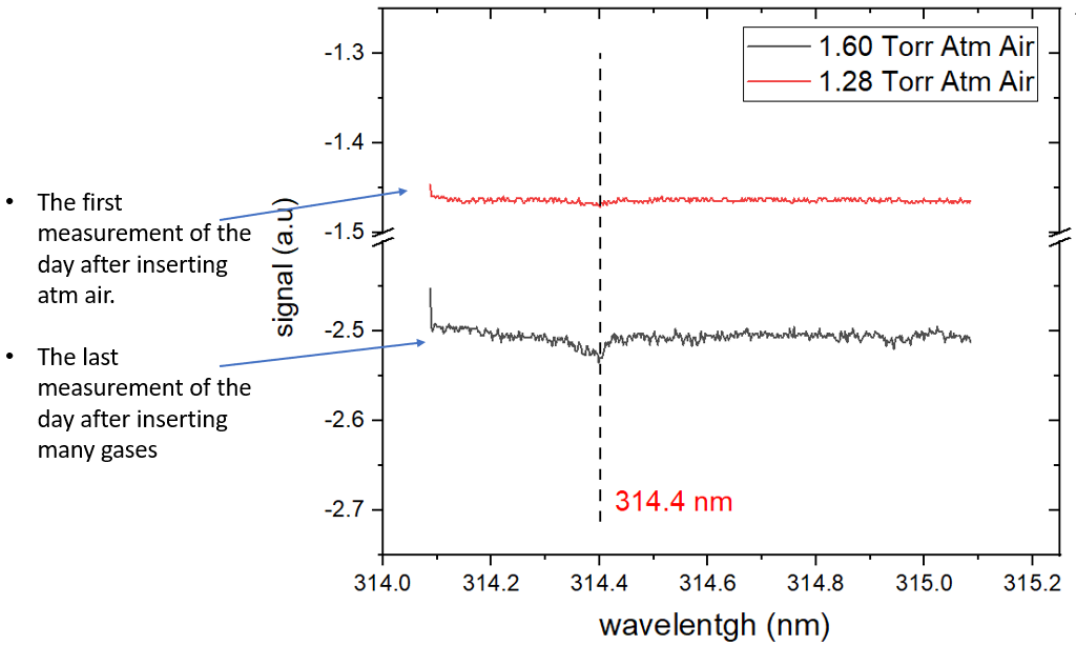

FIGURE 4.7: Ionization signal as a function of the wavelength at different times.

4.1.2 LC6100 - LC 5900 scans (278-307 nm)

In this sub-section, we are going to discuss ionization studies performed using the dye compounds LC6100 and LC5900 in the range $278 - 289$ and $292 - 307$ nm respectively. Before we show the spectra in this particular region, let's turn back to Figure 4.1 and identify the states accessible and within reach with our dye laser.

As shown in Figure 4.1, $\tilde{C}^1\Pi_u$ is the first Rydberg state with energy 8.16 eV. Although $\tilde{C}^1\Pi_u$ is within reach with the dye laser LC6100, the excitation from the ground state to this Rydberg state is forbidden via a 2 photon absorption and thus, ionization signal is not expected with a 2+1 photon absorption. Even if the transition to this state is forbidden with a 2 photon absorption, it is possible to access this state (but not obtain the ionization spectra) with the presence of low-lying ungerade $C - H$ bend mode ν_5 at 730 cm^{-1} [33] (this vibrational normal mode correspond to the ground state). Moreover, $3p^1\Pi_u$ has a highly dissociating character with lifetime around 47 fs [34]. The temporal window of our measurement is similar to the pulse duration (6 ns) making the state pre-dissociating as the molecule initiates fragmentation before ionization occurs. If this state was accessible in our experiment, we would expect a 2+1 multiphoton ionization signal at around 307 nm.

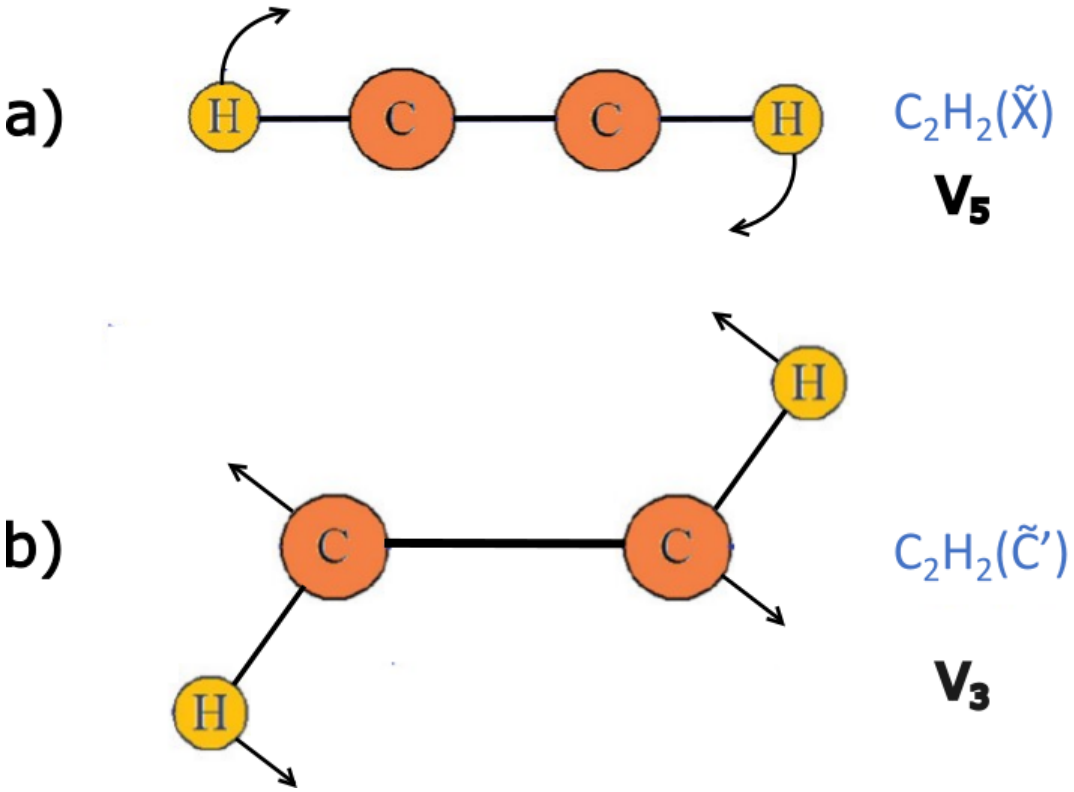

FIGURE 4.8: Schematic representation of: a) the ν_5 normal mode of the ground state of acetylene and b) the ν_3 trans-bend normal mode of the $C_{2\nu}$ excited acetylene [38].

Another highly pre-dissociating state within reach is the $3p^1\Pi_g$. To the best of our knowledge, this state has yet to be observed with a calculated energy of 8.433 eV [16] as shown in Figure 4.1. Both states have a linear geometry with slightly

different bond lengths [16]. Even though none of these states is detectable in our ionization experiment, we show the spectra for completion purposes on Figure 4.9.

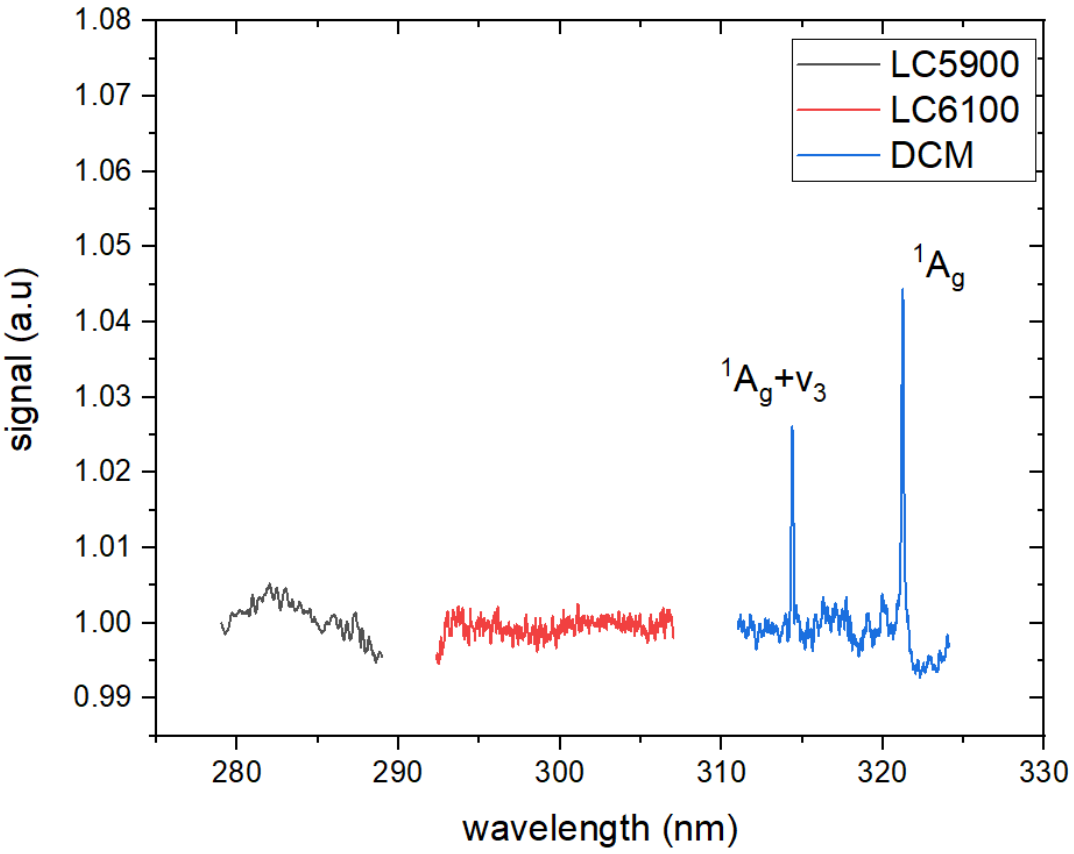

FIGURE 4.9: Calibrated 2+1 multiphoton ionization spectra of acetylene regarding the second harmonic of the 3 dye lasers. Black line: LC5900, Red line: LC6100, Blue line: DCM.

As expected, no ionization signal was observed in the spectral areas $279 - 289$ and $282 - 307$ nm. Both in LC5900 and LC6100 the pulse energy remained unchanged at 1.1 mJ while the initial pressure inside the cell was 1.5 Torr. In the LC5900 scan, pressure was increasing very fast so we had to break the scan into smaller parts and combine all of them at the end. That is the main reason behind the strange shape of the signal at this scan. In the next chapter we will analyze the results of the photooxidization experiment.

4.2 Photooxidation - Results

In this section, we are going to present the results extracted from the photooxidation experiment. Before we start discussing each spectral region, we will first present all the results of the photooxidation experiment regarding the reaction rate (κ). To keep the text simplified we make the correspondence between laser dye and spectral region as follows (no use of the Autotracker):

- DCM: $310 - 325$ nm

- LC6100: $284 - 307\ nm$
- LC5900: $270 - 280\ nm$.

According to both Figure 4.1 and the results from our multiphoton ionization experiment, $\tilde{C}^{1}A_g$ state lies inside the range of the DCM dye that we are using. Previously, we mentioned that both absorption and reactivity depends on the wavelength of the incoming radiation. Indicatively, we present on Figure 4.10 the time evolution of glyoxal absorption as extracted from the Mathematica software and show the dependency of the phenomenon on the wavelength of the laser.

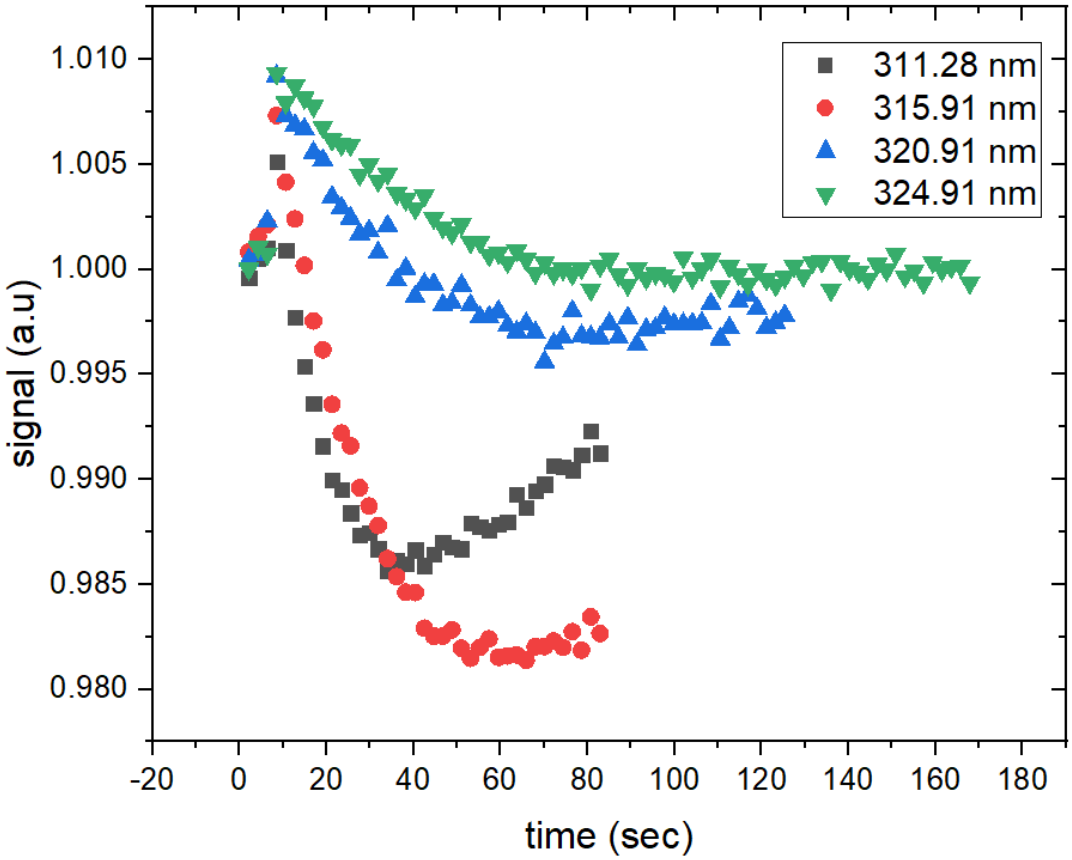

FIGURE 4.10: Time evolution of glyoxal absorption for different wavelengths of laser radiation

For the purposes of our work, we are only interested in the creation of glyoxal until it reaches its maximum value. In order to quantify the process, we extracted the reaction rate κ as described in sub-section 3.3.1 by fitting our data to the formula shown in Eq. 3.2.

Our study is comprised of several sets of measurements and in order to limit the error as much as possible, we measured the intensity both before and after the cell without the presence of the broadband source. Each measurement lasts a few minutes so we had to measure the pulse energy both before and after the measurement. If a significant change in the pulse energy was detected, the measurement was performed again. The pulse energy used in this series of experiments was kept close to

0.7 mJ. Figure 4.11 shows the results of our measurements showcasing the reaction rate of the photooxidation reaction in the glyoxal production channel.

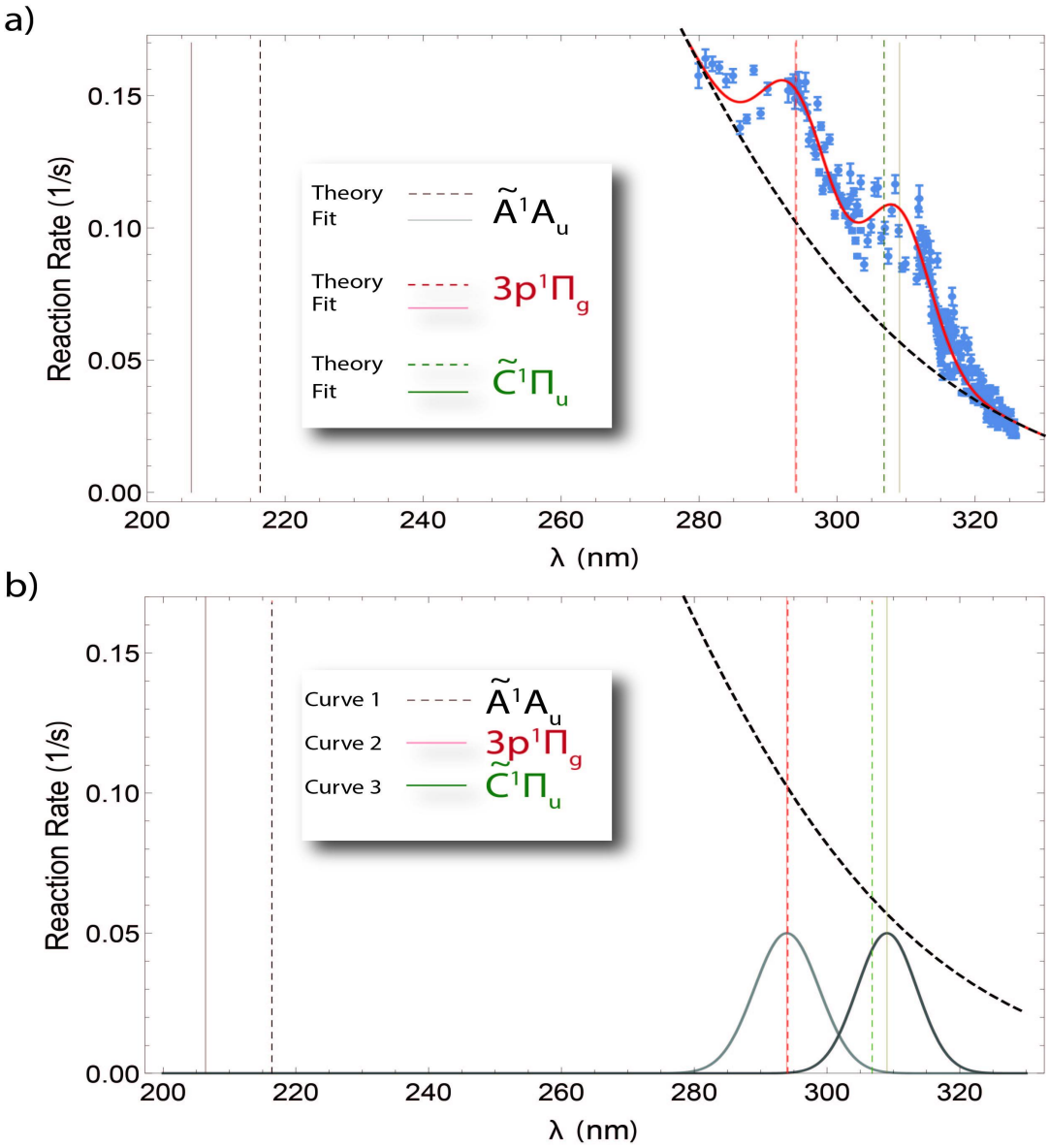

FIGURE 4.11: a) Reaction rate vs wavelength and fit with Eq. 4.1. b) Separate plots of the Gaussian curves contained in (a).

In the spectral region between $315 - 325$ nm, the reaction rate seems to drop almost linearly in contrast with the region below 315 nm where the scattering of the reaction rate increases just around the $^1\Pi_u$ Rydberg state. No change is observed in the neighborhood of the $\tilde{C}'^1A_g$ (around 320 nm) regarding the reaction rate showing no particular impact of this state in the photooxidation of acetylene. On the other hand, regarding the reaction rate, the gradient seems to slightly change near the second line at 314.4 nm around the $\tilde{C}'^1A_g + v_3$ line which is also noticed in Figure 4.11a. The difference between these 2 lines may correspond to the fact that $\tilde{C}'^1A_g$ is a stable Valence state while adding a vibration v_3 to this state inserts a partially

dissociating character (type II pre-dissociation according to Herzberg [26]) which possibly affects the whole process.

According to Figure 4.1, both $3p^1\Pi_g$ and $^1\Pi_u$ are within reach via a 2 photon absorption. In fact, $^1\Pi_u$ Rydberg state is forbidden via a 2 photon absorption process making the $3p^1\Pi_g$ Rydberg state the only state to be accessed through purely electronic excitation. On the previous chapter, we mentioned that both states have a pre-dissociating character (life time on the order of fs) as the molecule initiates fragmentation through conical intersection processes [26]. Both of these states are projected in Figure 4.11 but, due to the fact that these lines lie on the edges of the spectra (LC6100), we cannot observe any significant change in their neighborhood. On the other hand, the LC5900 datasets ($280-290\,nm$) reveal a small spectral plateau where the reaction rate of the photooxidation remains almost constant.

Now, we will attempt to quantify the reaction rate of the photooxidation of acetylene in order to shed light into the mechanism responsisble for the photooxidation process. Although Figure 4.11b shows the $\tilde{C}^1\Pi_u$ Rydberg state accessed by a 2 photon absorption process, the direct transition to such a Rydberg state from the ground state is only allowed with the absorption of odd number of photons due to selectivity rules. Adding the effect of vibrational excitation can lead to hot-bands in the absorption spectra in room temperature [7]. In fact, the low-lying ungerade C-H bend mode at 730 $cm^{-}1$ [33] should be taken into consideration as it is expected to participate in the reaction [4]. Thus, the absorption of 2 photons from the excited C-H bend mode (hence v_5 normal mode) of the ground electronic state activates the process of exciting acetylene molecules to the $\tilde{C}^1\Pi_u$ Rydberg state.

In order to elucidate the photooxidation mechanism we first fit our data with the following formula:

$$R(\lambda) = C\big(G(\tilde{A}^1A_u) + G(3p^1\Pi_g) + G(\tilde{C}^1\Pi_u - v_5)\big) \tag{4.1}$$

with C being a free fit parameter and $G(X)$ being a Gaussian function of the form:

$$G(X) = Ae^{-\left(\frac{\lambda-\lambda_X}{\Delta_X}\right)^2} \tag{4.2}$$

where A is the height of each Gaussian function, and λ_X, $\Delta\lambda_X$ are the two-photon resonant wavelength and the linewidth of each state considered, and which are left as free fit parameters. Figure 4.11 shows the result of such a fit. The nominal values for the resonant wavelengths are shown with dashed lines, while the fit results are indicated with solid lines in Figure 4.11a. In Figure 4.11b, we see each of the Gaussian curve, according to Eq. 4.2, plotted separately.

The theoretical values for $\lambda_{\tilde{A}^1A_u}$, $\lambda_{\tilde{C}^1\Pi_u}$ and $\lambda_{3p^1\Pi_g}$ are found in Figure 4.1 (theoretical predictions), while the value of the vibrational energy v_3 is found in [33] (experimental values). Using the $\Delta\lambda_{3p^1\Pi_g}$ and $\Delta\lambda_{\tilde{C}^1\Pi_u}$ values extracted from the fit we can estimate the lifetimes $\tau_{3p^1\Pi_g}$ and $\tau_{\tilde{C}^1\Pi_u}$ of the corresponding states. A value

for $\tau_{\tilde{C}^1\Pi_u}$ has been reported in [34] to be 47 fs, while there is no value for $\tau_{3p^1\Pi_g}$ since, to the best of our knowledge, this state has not been observed experimentally. The values for $\tau_{\tilde{C}^1\Pi_u}$ and $\tau_{3p^1\Pi_g}$ extracted from our data are 5 times smaller. However, the data presented in Figure 4.11, are in no way a spectroscopic study, but a study of reactivity, thus it is possible that additional, experimentally induced broadening mechanisms might contribute to the observed linewidths.

4.3 Photooxidation Mechanism

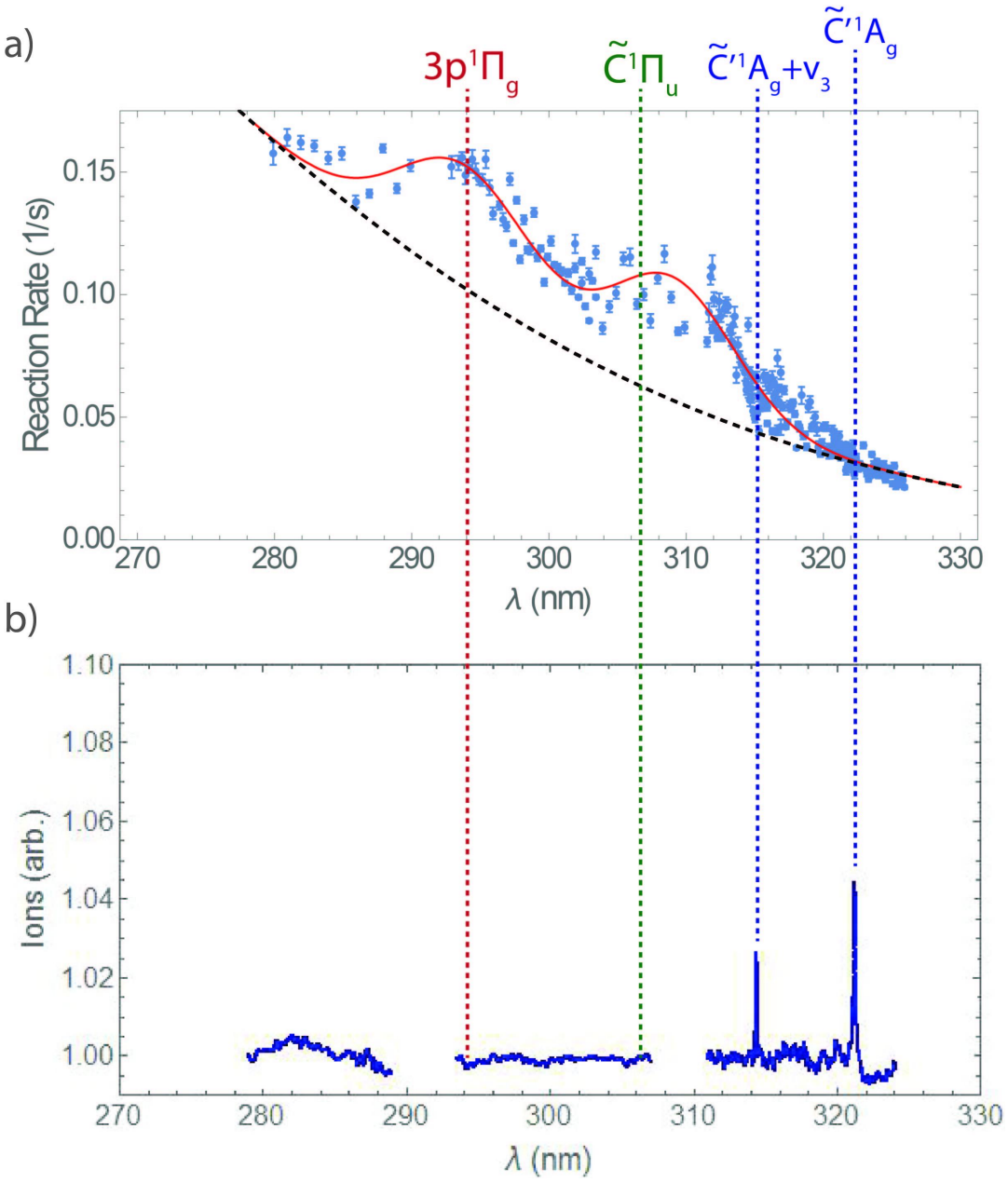

FIGURE 4.12: a) Reaction rates vs wavelength and fit with Eq. 4.1. b) Ionization rate as a function of the wavelength.

In this section we will try to elaborate on the photooxidation mechanism. In Figure 4.12, we see again the evolution of the reaction rate as a function of the wavelength and we compare it to the ionization rate versus wavelength. The $3p^1\Pi_g$ and $\tilde{C}^1\Pi_u$ are known to be absent in ionization experiments due to rapid dissociation. However, in the ionization spectra another state, the $\tilde{C}^1A_g$ is detected, along with a line at the wavelength corresponding to the excitation energy of $\tilde{A}^1A_u + v_3$. In this case, nominal values for the $\tilde{C}^1A_g$ and E_{v_3} are found in [38] (experimental investigation using UVODR spectroscopy). It is apparent that excitation to the rapidly pre-dissociating $3p^1\Pi_g$ and $\tilde{C}^1\Pi_u$ increases the photooxidation reactivity, while the $\tilde{C}^1A_g$ is not observed to significantly contribute to the reaction.

Which mechanism is responsible for the different contribution between the $3p^1\Pi_g$, the $\tilde{C}^1\Pi_u$ and the $\tilde{C}'^1A_g$ states to the photooxidation reaction? Is the molecule more reactive while being excited to a Rydberg state or is it more reactive after first being led to dissociation? The 2^{nd} scenario leads to the creation of free neutral C_2H radicals. Hay and Norish [9] observe glyoxal in their experiment in which they mix Acetylene and molecular Oxygen without the presence of a laser system and measure the pressure of each product by changing the temperature inside the chamber. They propose that the glyoxal formation is the product of the following reaction:

$$CH_2CHO + O_2 \rightarrow (CHO)_2 + OH \tag{4.3}$$

where the CH_2CHO is produced by the following reaction [9]:

$$C_2H_2 + OH \rightarrow HC = CH(OH) \tag{4.4}$$

where the $HC = CH(OH)$ can exist in the tautomeric form [9] CH_2CHO leading to glyoxal formation through a chain reaction mechanism. Bowman et al. [61] discusses the mechanisms (pathways) of the chemical reaction between ethynyl radical C_2H with molecular Oxygen. More specifically, they mention that the pathway S_3 ends up with the production of $HCCOO$ four-membered ring radical (see Figure 4.13). The addition of a neutral hydrogen to the reaction pathway produces glyoxal ($CHOCHO \rightarrow (CHO)_2$). In our experiment, the transition to both states $\tilde{C}^1\Pi_u$ and $3p^1\Pi_g$ drives acetylene to dissociation through the following pathway:

$$C_2H_2 \rightarrow C_2H + H \tag{4.5}$$

which leads to the production of the C_2H radical needed to initiate the reaction. Kalaitzis et al. [4] performed the same experiment around 220 and 320 nm. Regarding the spectral range around 320 nm the results were in good agreement with those that came up in our experiment. The reaction time in the spectral range around 220 nm is way lower than the reaction time observed near the 320 nm spectral region. The intensity difference between 320 and 220 nm is an order of magnitude due to the fact that the latter spectral region is accessed via single photon absorption.

Although the state is accessed through single photon absorption, the reaction time (glyoxal production) is much slower which is attributed to the fact that more than one dissociative channels participate reducing the amount of C_2H needed for the production of glyoxal as shown on sub-section 2.4 and [35].

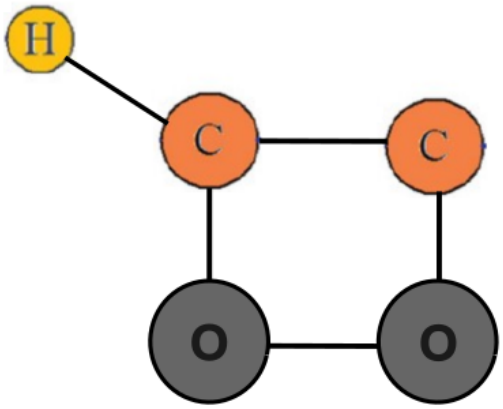

FIGURE 4.13: Qualitative representation of the four-membered ring produced in the S_3 pathway.

On the work done by Kalaitzis and co-workers, the reaction time is plotted as a function of the single photon energy. After a linear fit (we focus on the study around 220 nm) and an extrapolation process around $\tau = 0$ sec, the single photon energy that arises is 5.72 eV which is exactly the energy stated in [35] where the dissociating channel concerning the C_2H radicals production (through dissociation) appears. In their work, they used 193 nm laser radiation which corresponds to about 6.5 eV and found the that the dominant channel of dissociation is the first (85%). This leads us to believe that the more we reduce the wavelength of the incoming radiation, the more we increase the possibility of different channels participating in the reaction and thus, shutting down the glyoxal production (less C_2H produced means less glyoxal).

Chapter 5

Conclusions

In this work, we studied the photooxidation of acetylene using tunable UV radiation in the spectral range of $280 - 325\ nm$. Mainly, 2 experimental setups were used to extract the multiphoton ionization spectra and the time evolution of the absorption of glyoxal respectively. The first experiment revealed 2 ionization lines attributed to the $C'\ ^1\tilde{A}g$ Valence state around 321.2 and 314.4 nm via a 2+1 absorption process (where the +1 photon ionizes the molecule). The first line corresponds to a direct transition from the electronic ground state $\tilde{X}\ ^1\Sigma_g^+$ to the $C'\ ^1\tilde{A}g$ Valence state, while the second one corresponds to the transition from the ground state to the excited trans-bend vibrational state $\tilde{C}'\ ^1Ag + v_3$. The energy of this vibration was calculated to 1354 cm^{-1} which is in good agreement with previous theoretical [39] (2% shift) and experimental works [38] (4% shift). Applying a Lorentzian fit to the peaks, revealed a lifetime of around 1 ps very close to previous works [38].

Now, regarding the second experiment, photooxidation seems to initiate after excitation to a predissociating Rydberg state which gives rise to neutral C_2H radicals. The Rydberg states observed to impact the process are $3p^1\Pi_g$ and $\tilde{C}^1\Pi_u$ with lifetime around 50 fs, values that are 5 times greater than those observed in our experiment. The direct excitation to the latter Rydberg state is forbidden and only allowed assisted via vibrational excitation as well. The vibration that appears to be present is the trans-bend v_5 normal mode at 730 cm^{-1}. Our research is by no means a spectroscopic study but a study of reactivity which implies that further lifetime broadening mechanisms may take place. The absence of these 2 lines in typical ionization experiments is attributed to their pre-dissociating character which minimizes the chances of detection.

We conclude that the photooxidation reaction mainly proceeds though reaction of oxygen molecules and the radicals produced by dissociation. The predissociation mechanism that results to the small lifetimes of the $3p^1\Pi_g$, and $\tilde{C}^1\Pi_u$ states, and which prevents their detection using conventional ionization spectroscopy is what mainly drives the reaction. Additionally, the width of the spectral feature of these states appearing in the reactivity study reported here, might suggest that the reaction can take place in the early stages of the dissociation process, i.e at relatively small C-H distances. Reacting during the early stages of the dissociation process might further decrease the lifetime of the Rydberg states, a fact that could explain

the increased linewidths observed in the reaction rate experiment.

However, the non-silent $\tilde{C}^1A_g$ state is also considered to be predissociative, albeit of a different type. The $3p^1\Pi_g$, and $\tilde{C}^1\Pi_u$ states are believed to undergo Herzberg type I predissociation [26], were dissociation proceeds via crossings between electronic states, and is very fast. On the other hand, the $\tilde{C}^1A_g$ state is believed to undergo Herzberg type II pre-dissociation [26]. This process proceeds through vibrational excitation and it is in general much slower. The lifetime of the $\tilde{C}^1A_g$ state has been found to be on the order of ps [38], a value that is in accordance with the lifetimes we extract using the ionization linewidth in our experiment ($\approx 1ps$). The much larger lifetime of the $\tilde{C}^1A_g$ state indicates that predissociation of this state is much less efficient compared to predissociation in the $3p^1\Pi_g$, and $\tilde{C}^1\Pi_u$ states, and this indication is in agreement with our observation that ns ionization of the $\tilde{C}^1A_g$ state is efficient, while ns ionization of the $3p^1\Pi_g$, and $\tilde{C}^1\Pi_u$ states is not (i.e the fact that the $\tilde{C}^1A_g$ state is not silent). Overall, we believe that these results strongly indicate that the acetylene photooxidation reaction mainly proceeds via fragmentation, end they elucidate the role of the Rydberg and Valance states accessible in the 280-325nm.

Before closing this thesis text, we would like to make some proposals for further investigation regarding the photooxidation of acetylene. In order to have a better insight on the time evolution of the reaction pathways, someone has to use different broadband sources of radiation so the time evolution of the absorption spectra of more products could be monitored. Moreover, the reaction rate study until the first dissociative Valence state $\tilde{A}^1A_u$ (spectral region $220 - 280\ nm$) is necessary in order to validate the assumption of the S_3 reaction pathway that the C_2H radical follows by reacting with O_2 to form glyoxal. As the wavelength of the incoming radiation decreases the dissociating channel changes according to sub-section 2.4 and [35] which minimizes the production of C_2H radicals and will probably have an effect in the production of glyoxal. Another interesting approach is to use a fs pulse to drive the reaction (despite the large spectral width) in order to minimize the vibrational excitation via crossings that occur continously during the 6 ns long pulse. Last but far from least is to make a VMI study of the acetylene in multiple spectral regions that will reveal all kind of Rydberg states by monitoring the Freeman resonances that will appear in the spectra. This technique, combined with a time of flight mass spectroscopy, will shed light to the dissociation pathways of the acetylene molecule.

Appendix A

Frequency Conversion Unit (FCU)

In this work, a frequency conversion unit was used to produce the 2^{nd} harmonic of the fundamental frequency of the dye laser in order to be able to record the multi-photon ionization spectrum of acetylene. This frequency conversion unit comes with an Autotracking system that helps us automate the 2^{nd} harmonic production while scanning the permissible wavelengths of the dye laser. Figure A.1 shows the Auto-tracker system. The role of the compensator is to correct the direction of the laser

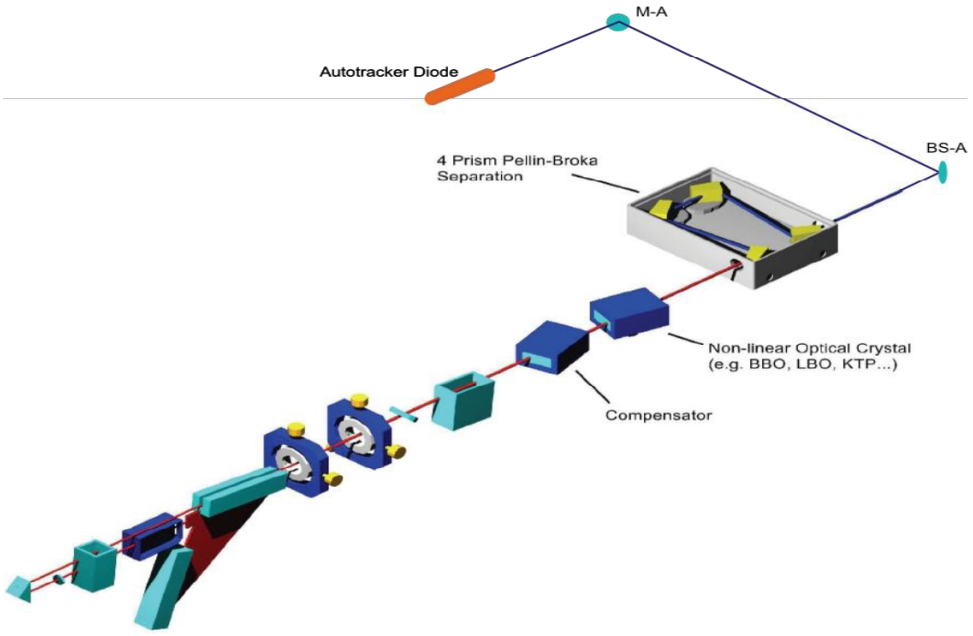

FIGURE A.1: Schematic illustration of the individual parts of the Autotracker.

beam so that it always falls into the center of the nonlinear BBO crystal to produce the 2^{nd} harmonic. After the 2^{nd} harmonic has been produced, it must be separated from the fundamental by a system of 4 pellin Broka prisms. The 2^{nd} Harmonic is driven to the BS-A beam splitter where one part is directed outside the FCU, while the other part of the beam ends in the Autotracker Diode.

A.1 Operation of the Autotracker

The Autotracker can operate in 2 independent ways when it comes to scanning. In order to understand the process, we should mention at this point that the base of both the Compensator and the BBO Crystal are rotated with the help of a motor which has 3×10^5 positions for the completion of a full rotation. Each step-position corresponds to 0.0012°. The 1^{st} way is through lookup tables, where the user stores in a table the wavelength and step-position of the crystal so that when loading this table on the Autotracker, it finds the optimal position of the 2 motors to produce the $2^{\eta\varsigma}$ harmonic. In our case this was not possible, as this method requires compatibility of the dye laser with the FCU. The 2^{nd} mode exploits the photodiode which is depicted in Figure A.2.

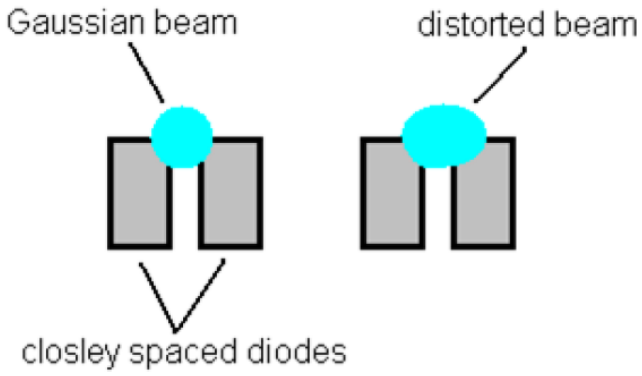

FIGURE A.2: Qualitative representation of the 2 area photodiode.

The Autotracker takes advantage of the distortion of the beam shape when the optically nonlinear production process of the 2^{nd} Harmonic is no longer in the optimal phase matching state. Under ideal conditions, the beam has a Gaussian profile upon the 2 area photodiode. If the wavelength of the laser changes by a small fraction(e.g. upon scanning), then the phase matching condition is not satisfied, and the beam is distorted either to the left or right, showing a higher intensity on one side compared to the other. This distortion can be quantified and exploited to generate an error signal, which is driven towards the motor of the BBO and Compensator. Thus, the Crystal rotates simultaneously and automatically while the laser scans, without using any former calibration (lookup tables).

To measure the beam distortion, (we actually measure positive-negative signal error) we use the so-called 2-area photodiode. Due to high intensity of the beam, there is always the risk of burning out the photodiode. To overcome this, we use only a small reflection. The reflection is driven to the center of the photodiode resulting in the measurement of the same signal spliited equally to the 2 areas of the photodiode. If the beam is now distorted, one area measures more signal. The signal from both regions is directed to the FCU, the magnitude of the difference and the sign of this deformation is calculated, so the motor is properly turned to bring the crystal back

to the appropriate angle to satisfy the phase matching condition and minimize the difference in the 2 areas of the photodiode.

A.2 Reliability of the Autotracker

To test how reliable the Autotracker (AT) is, it was considered necessary to study the conditions under which the AT can hold the 2^{nd} harmonic's intensity constant during the scanning process. For this purpose, 2 geometries were used with very different results.

A.2.1 Geometry A

In the present geometry, a reflection from the 2^{nd} Pelin Broka prism was used which is driven to the 2-area photodiode with the help of the beam splitter. This particular geometry failed due to geometry reasons. During scanning, when the wavelength of the fundamental beam changes slightly, the refractive index of the prism for the given wavelength changes, resulting in the beam being slightly deflected relative to the position it fell on the prism at the previous wavelength. This results in the constant shift of the beam onto the 2-area photodiode during scanning. Thus, the AT fails to satisfy the phase matching condition for the production of the 2^{nd} harmonic.

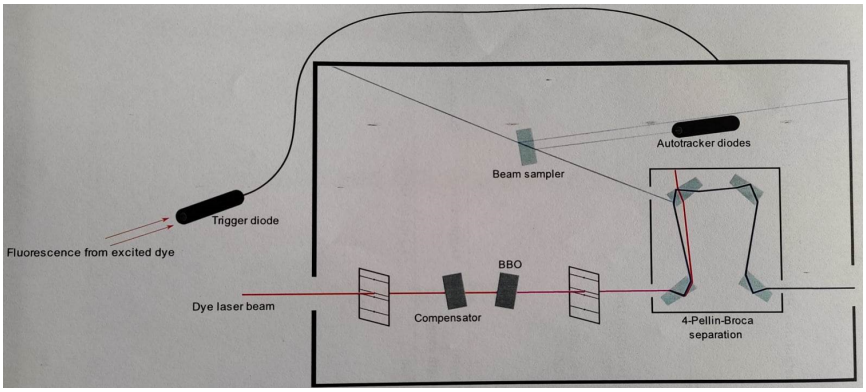

FIGURE A.3: Qualitative representation of Geometry A.

Figure A.4 represents the signal measured with the help of a external photodiode. In the case that AT was turned OFF, the signal from the 2^{nd} harmonic decreases almost linearly until it disappears, while in the case that the AT is turned ON, the signal drops immediately after 0.7 nm from the central wavelength of the scan. The scan was performed with a scan speed of 0.01 nm/s. Further study on the scanning velocity dependency revealed no dependency of the velocity in this geometry as far as it did not overcome 0.02 nm/s. The scan fails and cannot keep stable the output of the2^{nd} harmonic due to the continuous shifting of the beam, resulting in a breakdown of the reflection profile used by the 2-area photodiode. The photodiode is unable to send the appropriate signal to move the turning motor of both the BBO

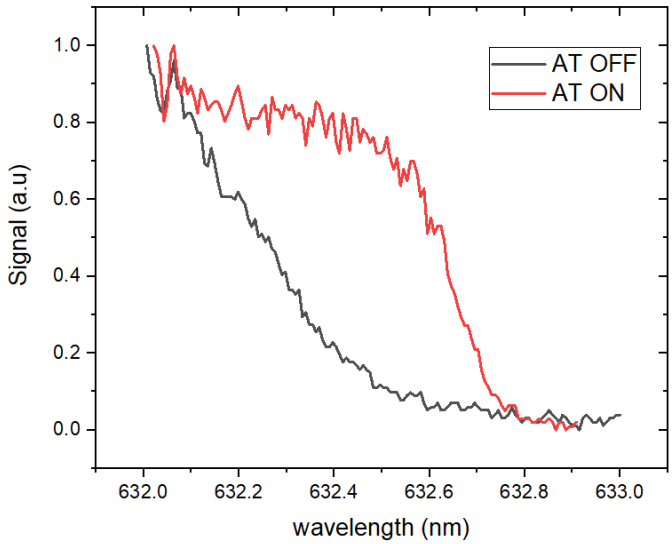

FIGURE A.4: Normalized signal in relation to the wavelength of the fundamental beam. In red, we show the scan in the presence of AT while in black we show the signal in the absence of the AT.

and the Compensator. This problem was overcome with the installation of geometry B, which is presnented in the next sub-section.

A.2.2 Geometry B

The problem that existed in geometry A was practically the continuous displacement of the beam reaching the 2-area photodiode. This problem can be treated with the geometry shown in Figure A.5. The displacement of the beam can be undone by

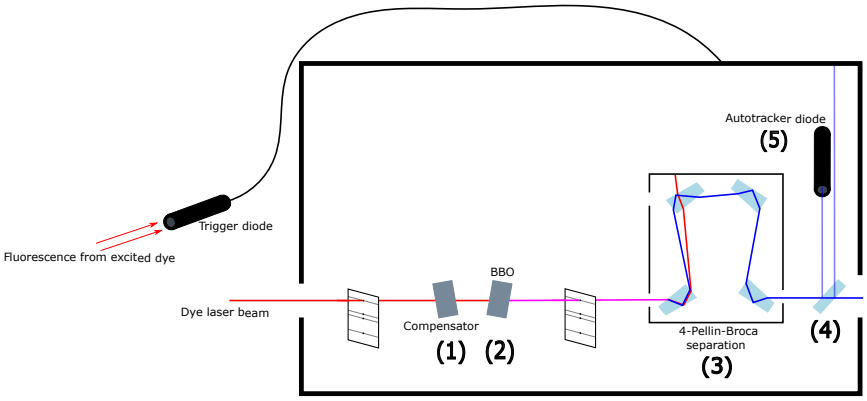

FIGURE A.5: Qualitative representation of Geometry B.

placing the beam splitter behind the 4-Pellin-Broca splitter by feeding the reflection of the front side of the beam splitter into the 2-area photodiode. In practice, the existence of 2 additional Pelin Broka prisms confers opposite displacement in relation to the first 2 prisms resulting in the extinction of any beam deviations and the reflection profile fed to the photodiode remains spatially stable.

To see the results of this particular geometry during scanning, we again placed a photodiode that would measure the intensity of the2^{nd} harmonic. The scan was

performed in a 6 nm range and the results are graphically represented in Figure **??** for various values of the threshold. The threshold is a factory setting of the AT that

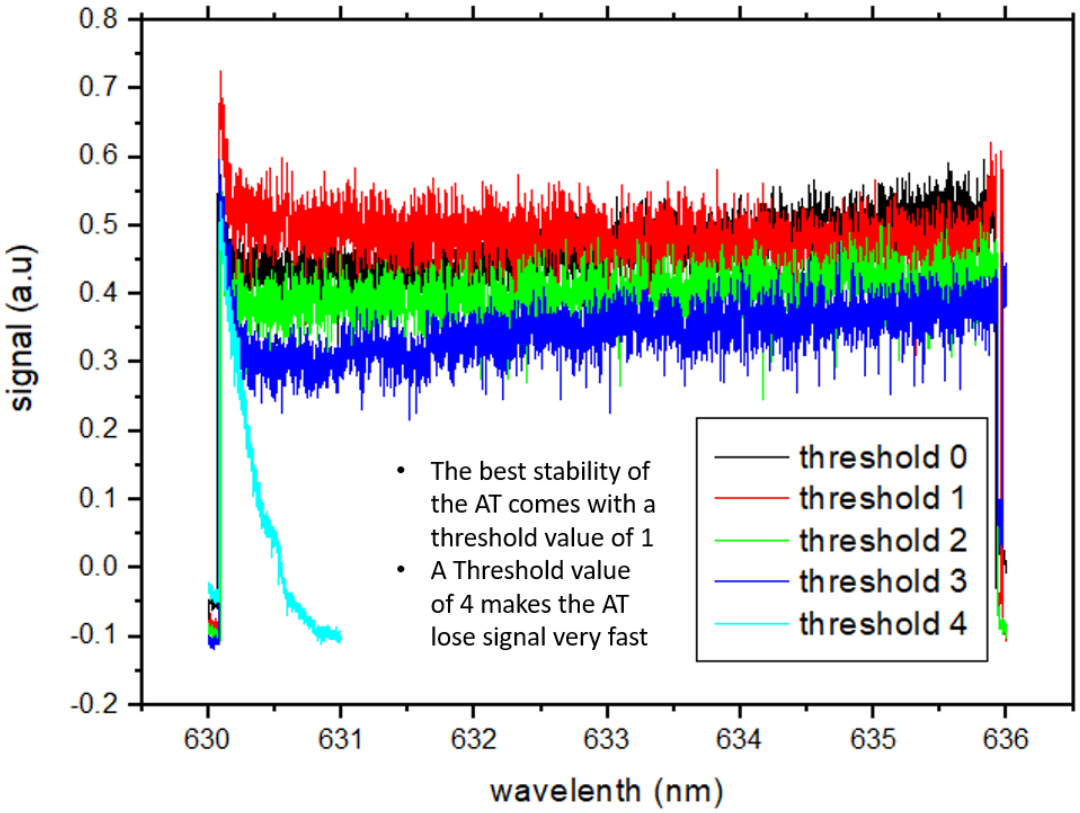

FIGURE A.6: $I = f(\lambda)$ of the 2^{nd} harmonic when scanning the fundamental beam in a range of 6 nm for various threshold values.

qualitatively determines when the command is given to turn the BBO. The 2-area photodiode, as was said earlier, sends the difference of signals it receives in the 2 regions. If the threshold is set to a large value, then the BBO Crystal will only turn when the difference in the signals sent by the photodiode exceeds the value set by the threshold. All 5 measurements were performed at the same scanning speed to arrive at the optimal setting. What we observed is that as we increased the Threshold, altought the AT continued to produce the 2^{nd} harmonic, it failed in terms of stability the same stability. For a threshold value 4 AT appeared to fail very quickly during the scan. Optimal stability conditions of AT were observed for threshold value of 1, which was held stable thereafter. Figure A.6 shows the scan for various threshold values.

In Figure A.7, we studied the response of the AT for different scanning velocities in different scanning regions. At first, what was observed was that the 0.02 nm/s step (which was also the big step) followed the dye laser profile better in terms of the intensity variations of the 2^{nd} harmonic. At this point, let us remind you that the lower axis is the wavelength of the fundamental beam and not the harmonic one. When the AT was operating at a 0.01 nm/s step, the fluctuations in the intensity were greater which also occurred at a 0.02 nm/s when we scanned a spectral area closer

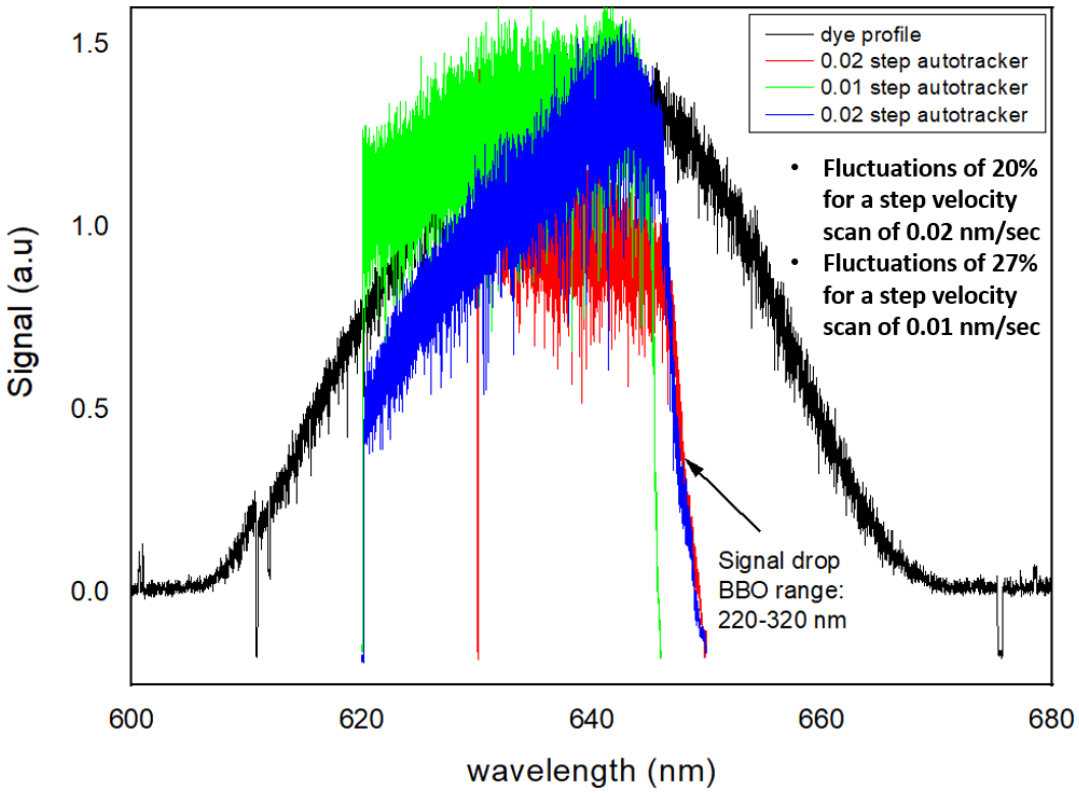

FIGURE A.7: $I = f(\lambda)$ of the 2^{nd} harmonic when scanning the fundamental beam in a range covering the entire dye laser for various scanning velocities.

to the dye's profile peak. Another equally important observation is that the AT fails in all 3 cases to hold the production of the 2^{nd} harmonic at the same spectral region. However, we believe that this is the outcome of 2 factors. The first has to do with the fact that the BBO crystal is designed to produce the 2^{nd} harmonic in the spectral region between $220 - 320\ nm$, while the second has to do with the fact that in that area there is a sharp decrease in the intensity of the fundamental beam and so the AT is unable to correct this decrease and as a result fails completely. Another interesting feature of AT that needs further investigation is the fact that it fails to carry out reverse scanning (from longer wavelengths to shorter). However, we believe that this problem is geometric and has to do with the difference signals sent to the AT to move the motor. That is, practically, AT may have a preference for the sign of the difference signals between the 2 photodiodes (software issue). It was previously reported that all 3 scans fail at a similar wavelength, and one possible reason is how steep the intensity decrease is at this point. It was observed, during the experiments, that the higher the intensity of the dye laser the more difficult it is for the AT to keep these variations in constant intensity, so it was considered necessary in some cases to work at lower scanning velocities ($0.005\ nm/s$). Figure A.8 shows the linear dependency of the position (of the BBO crystal) on the fundamental wavelength of the laser.

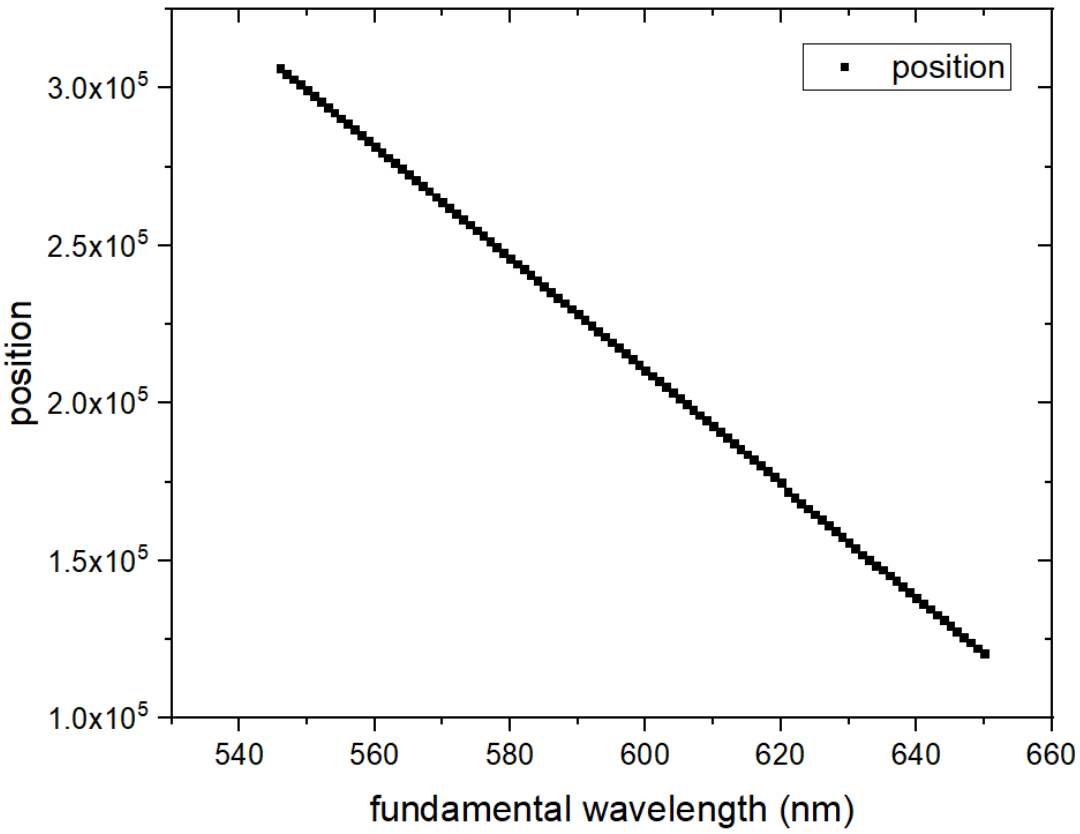

FIGURE A.8: Schematic representation of the linear dependency of the position of the BBO crystal on the fundamental wavelength of the laser.

Appendix B

Laser Dyes and specifications

All references can be found in [62].

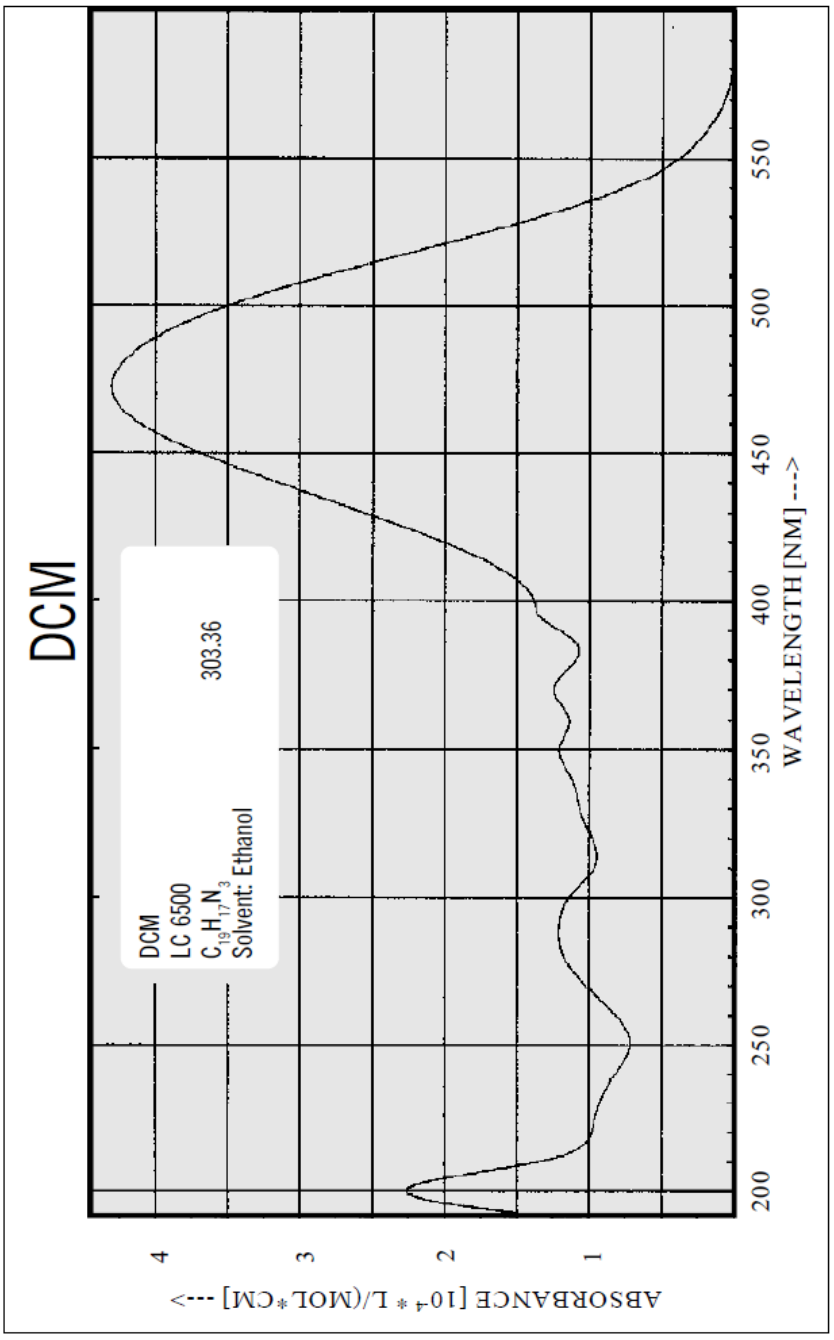

DCM (LC 6500)

Constitution

4-Dicyanmethylene-2-methyl-6-(p-dimethylaminostyryl)-4*H*-pyran

$C_{19}H_{17}N_3$ · MW: 303.36

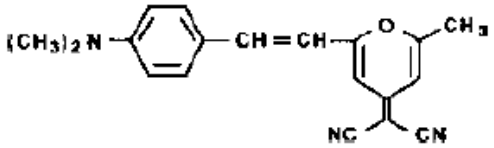

Characteristics

Lambdachrome® number:	6500
CAS registry number:	51325-91-8
Appearance:	red, crystalline solid
Absorption maximum (in ethanol):	472 nm
Molar absorptivity:	4.25 x 10^4 L mol^{-1} cm^{-1}
Fluorescence maximum (in ethanol):	644 nm

For research and development purposes only.

Lasing Performance

Efficient laser dye for pulsed and CW operation; tunable around 650 nm. DCM Special gives higher efficiency due to better solubility.

Pump		*Dye Laser Characteristics*					
Source	*Wavelength [nm]*	*Peak [nm]*	*Range [nm]*	*Effic. [%]*	*Conc. [g/l]*	*Solvent*	*Ref.*
XeCl-Excimer	*308*	*658*	*632 - 690*	*12*	*0.71*	*DMSO*	*1, 2*
Nitrogen	*337*	*659*	*626 - 703*	*rel.*	*0.50*	*DMSO*	*3*
Nd:YAG, 2nd	*532*	*639*	*615 - 666*	*27*	*0.50*	*PC*	*1, 4*
Cu-vapor	*510*	*644*	*598 - 677*	*14*	*0.61*	*Methanol*	*5*
Flashlamp	*-*	*655*	*610 - 710*	*-*	*0.76*	*DMSO*	*6, 7*
CW, Ar^+	*VIS*	*660*	*-*	*-*	*0.45*	*Bz./Eg.*	*1, 8, 9, 10*

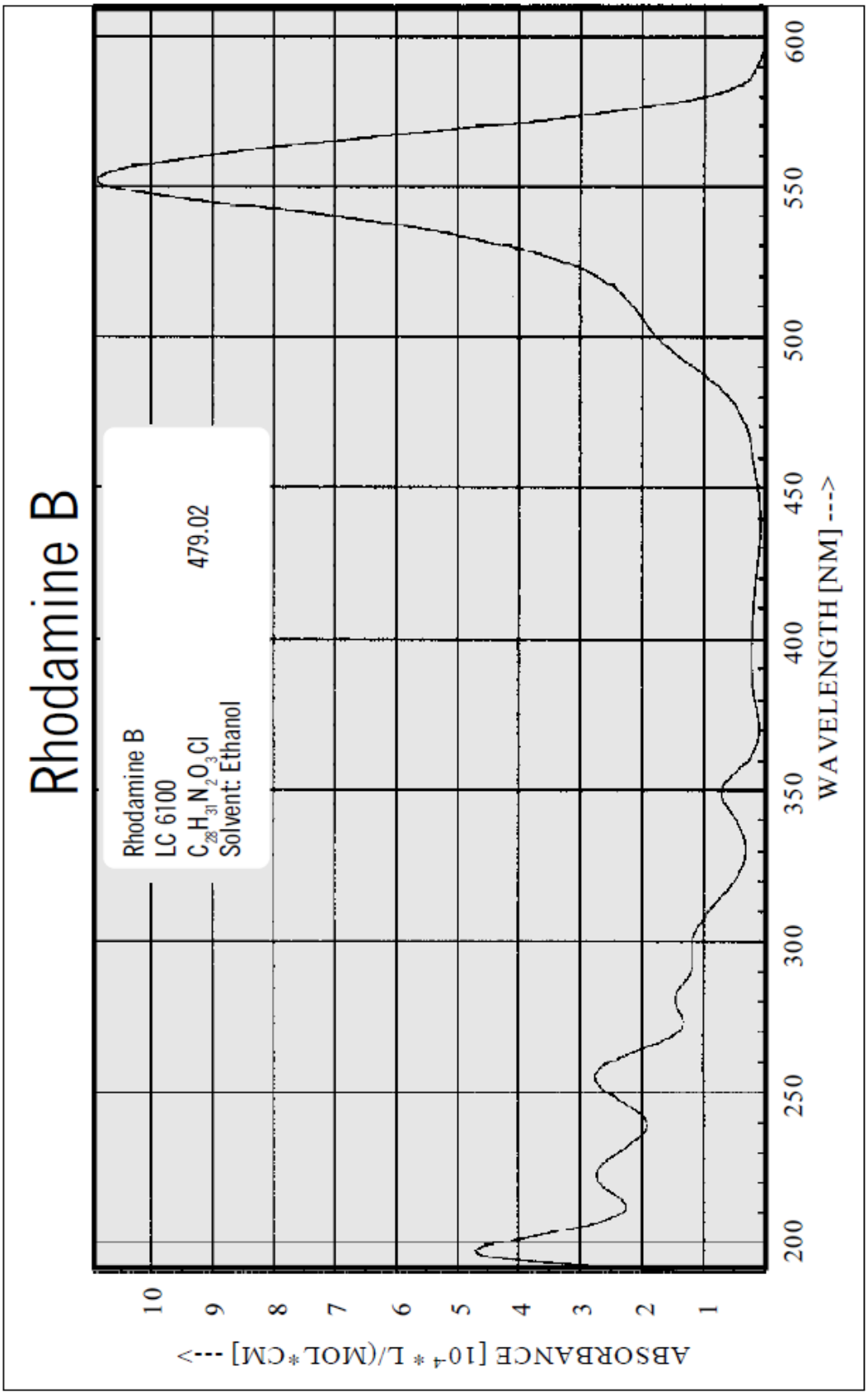
Rhodamine B
Rhodamine B
LC 6100
$C_{28}H_{31}N_2O_3Cl$
479.02
Solvent: Ethanol
ABSORBANCE [10^{-4} * L/(MOL*CM)] --->
WAVELENGTH [NM] --->
200
250
300
350
400
450
500
550
600
1
2
3
4
5
6
7
8
9
10

Rhodamine B (LC 6100)

Constitution

2-[6-(Diethylamino)-3-(diethylimino)-3H-xanthen-9-yl] benzoic acid
Rhodamine 610

$C_{28}H_{31}N_2O_3Cl$ · MW: 479.02

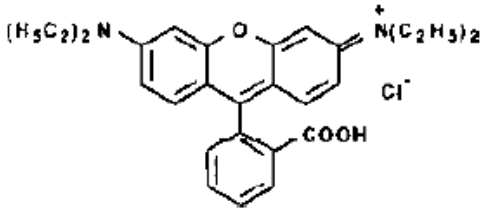

Characteristics

Lambdachrome® number:	6100
CAS registry number:	81-88-9
Appearance:	green, crystalline solid
Absorption maximum (in ethanol):	552 nm
Molar absorptivity:	10.7×10^4 L mol^{-1} cm^{-1}
Fluorescence maximum (in ethanol):	580 nm

For research and development purposes only.

Lasing Performance

Very efficient and frequently used laser dye for pulsed and CW operation; tunable around 610 nm.

Pump		*Dye Laser Characteristics*					
Source	*Wavelength [nm]*	*Peak [nm]*	*Range [nm]*	*Effic. [%]*	*Conc. [g/l]*	*Solvent*	*Ref.*
XeCl-Excimer	*308*	*600*	*588 - 644*	*12*	*0.91*	*Methanol*	*1, 2*
Nitrogen	*337*	*622*	*599 - 650*	*rel.*	*2.13*	*Methanol*	*2, 3, 4*
Nd:YAG, 2nd	*532*	*594*	*584 - 619*	*29*	*0.22*	*Methanol*	*1, 5, 6*
Cu-vapo	*510*	*591*	*582 - 618*	*21*	*0.62*	*Ethanol*	*7, 8*
Flashlamp	*-*	*618*	*590 - 640*	*-*	*0.05*	*Ethanol*	*9, 10*
CW, Ar^+	*all*	*640*	*605 - 675*	*-*	*3.53*	*MeOH/Eg.*	*11*

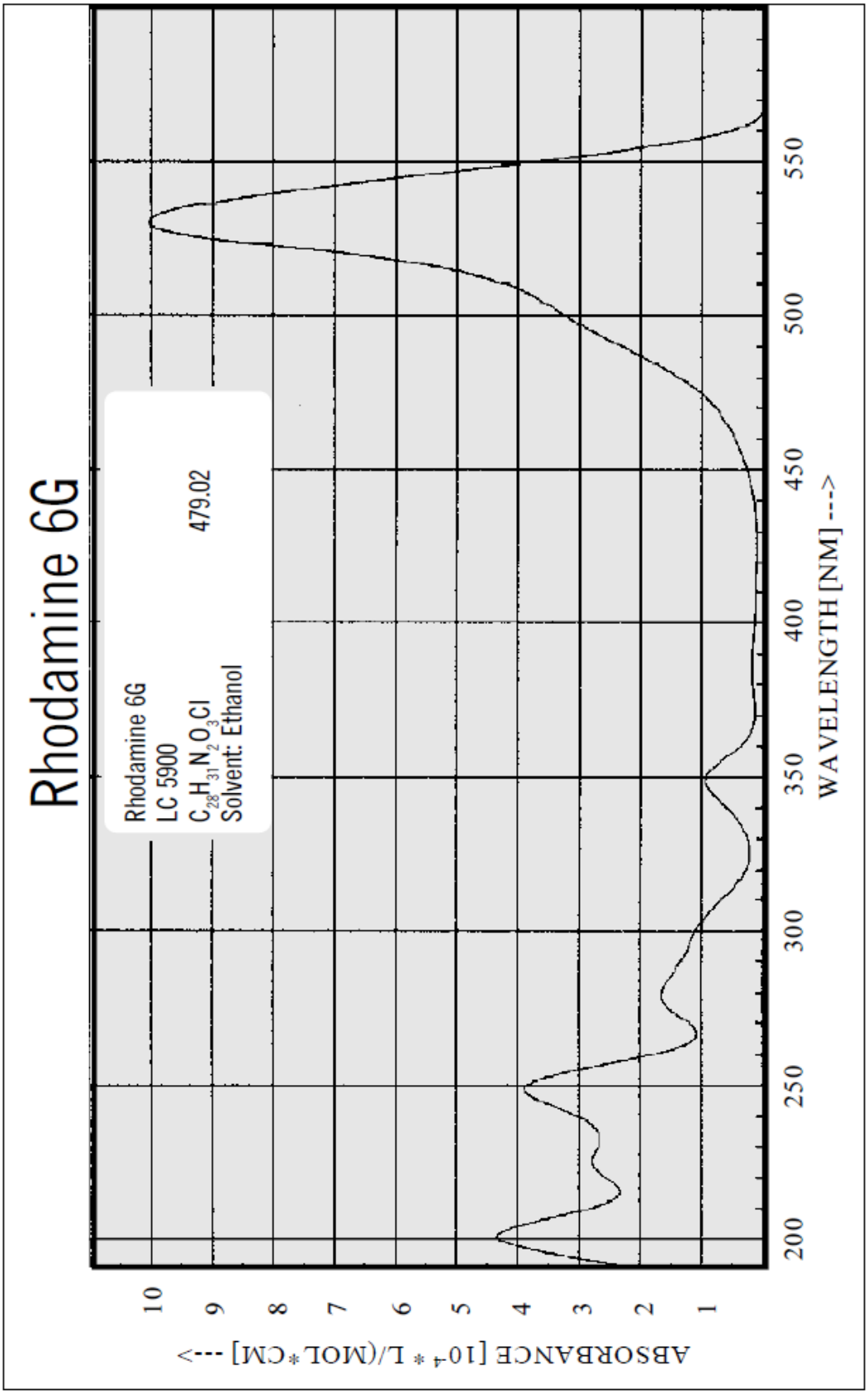
Rhodamine 6G
Rhodamine 6G
LC 5900
$C_{28}H_{31}N_2O_3Cl$
479.02
Solvent: Ethanol
ABSORBANCE [10^{-4} * L/(MOL*CM)] --->
1
2
3
4
5
6
7
8
9
10
200
250
300
350
400
450
500
550
WAVELENGTH [NM] --->

Rhodamine 6G (LC 5900)

Constitution

Benzoic Acid, 2-[6-(ethylamino)-3-(ethylimino)-2,7-dimethyl-3H-xanthen-9-yl]-ethyl ester, monohydrochloride
Rhodamine 590

$C_{28}H_{31}N_2O_3Cl$ · MW: 479.02

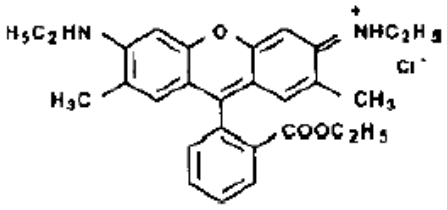

Characteristics

Lambdachrome® number:	5900
CAS registry number:	989-38-8
Appearance:	red, crystalline solid
Absorption maximum (in ethanol):	530 nm
Molar absorptivity:	10.50 x 10^4 L mol^{-1} cm^{-1}
Fluorescence maximum (in ethanol):	556 nm

For research and development purposes only.

Lasing Performance

The laser dye "per se" Rhodamine 6G is by far the most frequently used and most widely investigated laser dye. Very efficient laser dye for pulsed and CW operation; tunable around 590 nm.

Pump		*Dye Laser Characteristics*					
Source	*Wavelength [nm]*	*Peak [nm]*	*Range [nm]*	*Effic. [%]*	*Conc. [g/l]*	*Solvent*	*Ref.*
XeCl-Excimer	*308*	*581*	*569 - 608*	*16*	*1.20*	*Methanol*	*1, 2, 3*
Nitrogen	*337*	*581*	*573 - 618*	*rel.*	*1.63*	*Methanol*	*3, 4, 5*
Nd:YAG, 2nd	*532*	*566*	*555 - 585*	*32*	*0.10*	*Methanol*	*1, 6, 7*
Flashlamp	*-*	*600*	*555 - 620*	*-*	*1.20*	*Ethanol*	*9, 10*
CW, Ar^+	*all*	*575*	*560 - 625*	*-*	*0.75*	*Eg.*	*1, 11, 12, 13*

References

[1] Richard Dahlbom et al. "Acetylene Compounds of Potential Pharmacological Value. VIII. N-(4-Dialkylamino-2-butynyl)-Substituted Cyclic Imides1". In: *Journal of Medicinal Chemistry* 9.6 (1966), pp. 843–846.

[2] Judith A Bowman and John Bryan Willis. "Applications of the nitrous oxide-acetylene flame in chemical analysis by atomic absorption spectrometry". In: *Analytical chemistry* 39.11 (1967), pp. 1210–1216.

[3] Eric Herbst. "Chemistry in the interstellar medium". In: *Annual Review of Physical Chemistry* 46.1 (1995), pp. 27–54.

[4] Panagiotis Kalaitzis, Dimitris Sofikitis, and Constantine Kosmidis. "The role of predissociation states in the UV photooxidation of acetylene". In: *Journal of Photochemistry and Photobiology A: Chemistry* 436 (2023), p. 114373.

[5] CY Robert Wu et al. "Photoabsorption and direct dissociation cross sections of C2H2 in the 1530–1930 Å region: A temperature dependent study". In: *The Journal of chemical physics* 91.1 (1989), pp. 272–280.

[6] H Okabe. "Photochemistry of acetylene". In: *Canadian Journal of Chemistry* 61.5 (1983), pp. 850–855.

[7] Y Bénilan et al. "The long wavelength range temperature variations of the mid-UV acetylene absorption coefficient". In: *Planetary and Space Science* 48.5 (2000), pp. 463–471.

[8] BS Haynes, H Jander, and H Gg Wagner. "Optical studies of soot-formation processes in premixed flames". In: *Berichte der Bunsengesellschaft für physikalische Chemie* 84.6 (1980), pp. 585–592.

[9] JM Hay and Ronald George Wreyford Norrish. "The oxidation of acetylene". In: *Proceedings of the Royal Society of London. Series A. Mathematical and Physical Sciences* 288.1412 (1965), pp. 17–38.

[10] Sam J Silva, Colette L Heald, and Meng Li. "Space-Based Constraints on Terrestrial Glyoxal Production". In: *Journal of Geophysical Research: Atmospheres* 123.23 (2018), pp. 13–583.

[11] Christophe Lerot et al. "Glyoxal tropospheric column retrievals from TROPOMI–multi-satellite intercomparison and ground-based validation". In: *Atmospheric Measurement Techniques* 14.12 (2021), pp. 7775–7807.

[12] Tzung-May Fu et al. "Global budgets of atmospheric glyoxal and methylglyoxal, and implications for formation of secondary organic aerosols". In: *Journal of geophysical research: atmospheres* 113.D15 (2008).

[13] TM Stevenson and CFH Tipper. "The photo-induced oxidation of acetylene". In: *Combustion and Flame* 11.1 (1967), pp. 35–48.

[14] Bruce S Ault. "The 193-nm excimer laser induced photooxidation of simple alkynes in inert matrices". In: *The Journal of Physical Chemistry* 93.6 (1989), pp. 2456–2461.

[15] Alan N Arrowsmith, Viktor Chikan, and Stephen R Leone. "Dynamics of the CH (A2Δ) product from the reaction of C2H with O2 studied by Fourier transform visible spectroscopy". In: *The Journal of Physical Chemistry A* 110.24 (2006), pp. 7521–7526.

[16] Fabrice Laruelle et al. "Revisiting Mulliken's Concepts about Rydberg States and Rydberg- Valence Interactions from Large-Scale Ab Initio Calculations on the Acetylene Molecule". In: *The Journal of Physical Chemistry A* 113.47 (2009), pp. 13210–13220.

[17] TF Gallagher. "Rydberg Atoms, Cambridge University Press". In: *Cambridge, England* (1994).

[18] Mark Sheard Child. *Theory of Molecular Rydberg States*. Cambridge University Press, 2011.

[19] Attila Szabo and Neil S Ostlund. *Modern quantum chemistry: introduction to advanced electronic structure theory*. Courier Corporation, 2012.

[20] Peter W Atkins and Ronald S Friedman. *Molecular quantum mechanics*. Oxford university press, 2011.

[21] Jean-Michel Combes, Pierre Duclos, and Ruedi Seiler. "The born-oppenheimer approximation". In: *Rigorous atomic and molecular physics* (1981), pp. 185–213.

[22] Dimitrios Sofikitis. *Lecture notes in Molecular Physics*. 2020.

[23] Jean M Standard and Brian K Clark. "The Franck-Condon principle and Condon parabolas in a physical chemistry or quantum physics course". In: *Journal of chemical education* 76.10 (1999), p. 1363.

[24] Stuart Mackenzie. *Lecture notes in Molecular Physics*. 2020. URL: http://mackenzie.chem.ox.ac.uk/teaching.html.

[25] Makoto Takahashi, Masaaki Fujii, and Mitsuo Ito. "Two-color double resonance spectroscopy via A 1 A u state of acetylene: 3 p Rydberg state and its Renner–Teller effect". In: *The Journal of chemical physics* 96.9 (1992), pp. 6486–6494.

[26] Gerhard Herzberg. *The spectra and structures of simple free radicals: an introduction to molecular spectroscopy*. Courier Corporation, 1988.

[27] James AR Samson and RB Cairns. "Ionization Potential of O 2". In: *JOSA* 56.6 (1966), pp. 769–775.

[28] Marcus D Hanwell et al. "Avogadro: an advanced semantic chemical editor, visualization, and analysis platform". In: *Journal of cheminformatics* 4.1 (2012), p. 17.

[29] Jeffery A Greathouse. "Group Theory Calculations Involving Linear Molecules". In: *The Chemical Educator* 1 (1996), pp. 1–12.

[30] Tian Lu and Feiwu Chen. "Multiwfn: A multifunctional wavefunction analyzer". In: *Journal of Computational Chemistry* 33.5 (2012), pp. 580–592. DOI: 10.1002/jcc.22885. eprint: https://onlinelibrary.wiley.com/doi/pdf/10.1002/jcc.22885. URL: https://onlinelibrary.wiley.com/doi/abs/10.1002/jcc.22885.

[31] Papigkiotis Iraklis Marios. "Numerical calculations of Atomic Asymptotic coefficients using GAMESS". MA thesis. University of Ioannina, Greece, 2020.

[32] Michael W Schmidt et al. "General atomic and molecular electronic structure system". In: *Journal of computational chemistry* 14.11 (1993), pp. 1347–1363.

[33] Shimanouchi. *Acetylene Vibrational Modes*. https://webbook.nist.gov/cgi/cbook.cgi?ID=C74862&Units=SI&Mask=800. 1972.

[34] Yongwei Zhang et al. "Photodissociation dynamics of acetylene via the C Π 1 u electronic state". In: *The Journal of chemical physics* 133.1 (2010), p. 014307.

[35] S Satyapal and R Bersohn. "Photodissociation of acetylene at 193.3 nm". In: *The Journal of Physical Chemistry* 95.21 (1991), pp. 8004–8006.

[36] Michael NR Ashfold et al. "$\pi\sigma^*$ excited states in molecular photochemistry". In: *Physical Chemistry Chemical Physics* 12.6 (2010), pp. 1218–1238.

[37] Camille Sandorfy. *The role of Rydberg states in spectroscopy and photochemistry: low and high Rydberg states*. Vol. 20. Springer Science & Business Media, 2002.

[38] James K Lundberg et al. "Ultraviolet-Optical Double-Resonance study of the predissociated C 1Ag state of acetylene". In: *Journal of Molecular Spectroscopy* 156.1 (1992), pp. 104–122.

[39] Jacques Lievin. "Ab initio characterization of the C 1Ag state of the acetylene molecule". In: *Journal of Molecular Spectroscopy* 156.1 (1992), pp. 123–146.

[40] Masaaki Fujii, Akimitsu Haijima, and Mitsuo Ito. "Predissociation of acetylene in Ã 1Au state". In: *Chemical physics letters* 150.6 (1988), pp. 380–385.

[41] PD Foo and KK Innes. "Spectrum of acetylene: 1650–1950 Å". In: *Chemical Physics Letters* 22.3 (1973), pp. 439–442.

[42] Frank J Duarte. *Tunable laser optics*. CRC Press, 2017.

[43] BH Soffer and BB McFarland. "Continuously tunable, narrow-band organic dye lasers". In: *Applied physics letters* 10.10 (1967), pp. 266–267.

[44] François Kajzar and Vladimir M Agranovich. *Multiphoton and Light Driven Multielectron Processes in Organics: New Phenomena, Materials and Applications: Proceedings of the NATO Advanced Research Workshop on Multiphoton and Light Driven Multielectron Processes in Organics: New Phenomena, Materials and Applications Menton, France 26–31 August 1999*. Vol. 79. Springer Science & Business Media, 2012.

[45] ORTEC®. *Models 142A, 142B, and 142C Preamplifiers Operating and Service Manual*. English. Advanced Measurement Technology, Inc. 16 pp. 2002.

[46] Andor Shamrock. *Andor Shamrock 303i User's Guide*. English. Andor Technology Ltd. 16 pp. 20 Dec 2016.

[47] Andor Shamrock. *Andor Solis software Guide*. English. Andor Technology Ltd. 121 pp. 20 Dec 2016.

[48] Wolfram Research, Inc. *Mathematica, Version 11.3*. Champaign, IL, 2018.

[49] AS Zyubin and AM Mebel. "Accurate prediction of excitation energies to high-lying Rydberg electronic states: Rydberg states of acetylene as a case study". In: *The Journal of chemical physics* 119.13 (2003), pp. 6581–6587.

[50] Karsten Malsch et al. "Excited states of acetylene: a CASPT2 study". In: *Theoretical Chemistry Accounts* 100 (1998), pp. 171–182.

[51] Valérie Blanchet et al. "(3+ 1)-resonantly enhanced multiphoton ionization-photoelectron spectroscopy of the (3d-4s) supercomplex of acetylene: The geometry of the E state revisited through experiment and theory". In: *The Journal of chemical physics* 119.7 (2003), pp. 3751–3762.

[52] R Dressler and M Allan. "A dissociative electron attachment, electron transmission, and electron energy-loss study of the temporary negative ion of acetylene". In: *The Journal of chemical physics* 87.8 (1987), pp. 4510–4518.

[53] Michel Herman and Réginald Colin. "High resolution spectroscopic study of the Rydberg series of the acetylene isotopic molecules". In: *Physica scripta* 25.2 (1982), p. 275.

[54] Michael NR Ashfold et al. "G erade Rydberg states of acetylene studied by multiphoton ionization and photoelectron spectroscopy". In: *The Journal of chemical physics* 87.9 (1987), pp. 5105–5115.

[55] Michel Herman and Réginald Colin. "The absorption spectra of C2H2, C2D2, and C2HD in the region 1260 to 1370 Å". In: *Journal of Molecular Spectroscopy* 85.2 (1981), pp. 449–461.

[56] Michael NR Ashfold et al. "A 1Φ u Rydberg state of acetylene revealed by gas phase multiphoton ionization spectroscopy". In: *Molecular Physics* 56.5 (1985), pp. 1185–1199.

[57] JH Fillion et al. "Observation of the lowest 1Δ u Rydberg state of acetylene by multiphoton ionization spectroscopy". In: *The Journal of chemical physics* 105.1 (1996), pp. 22–30.

[58] Kazuhide Tsuji et al. "Spectroscopy and predissociation of acetylene in the np gerade Rydberg states". In: *The Journal of Physical Chemistry A* 106.5 (2002), pp. 747–753.

[59] Séverine Boyé-Péronne, Dolores Gauyacq, and Jacques Liévin. "Vinylidene-acetylene cation isomerization investigated by large scale ab initio calculations". In: *The Journal of chemical physics* 124.21 (2006), p. 214305.

[60] P Rupper and Frédéric Merkt. "Intense narrow-bandwidth extreme ultraviolet laser system tunable up to 20 eV". In: *Review of scientific instruments* 75.3 (2004), pp. 613–622.

[61] Michael C Bowman et al. "Mechanisms of the ethynyl radical reaction with molecular oxygen". In: *The Journal of Physical Chemistry A* 122.49 (2018), pp. 9498–9511.

[62] Ulrich Brackmann. "Laser dyes". In: *Göttingen (Germany): Lambda Physik AG. D* 37079 (2000).